nature communications

Article

https://doi.org/10.1038/s41467-024-54766-1

Directional ciliary beats across epithelia require Ccdc57-mediated coupling between axonemal orientation and basal body polarity

Received: 1 November 2023

Accepted: 19 November 2024

Published online: 26 November 2024

Check for updates

Xinwen Pan[1,2,7], Chuyu Fang[1,3,7], Chuan Shen[1,2,7], Xixia Li[4], Lele Xie[1], Luan Li[1,3], Shan Huang[1,3], Xiumin Yan[5] ✉ & Xueliang Zhu[1,2,3,6] ✉

Motile cilia unify their axonemal orientations (AOs), or beat directions, across epithelia to drive liquid flows. This planar polarity results from cytoskeleton-driven swiveling of basal foot (BF), a basal body (BB) appendage coincident with the AO, in response to regulatory cues. How and when the BF-AO relationship is established, however, are unaddressed. Here, we show that the BF-AO coupling occurs during rotational polarizations of BBs and requires Ccdc57. Ccdc57 localizes on BBs as a rotationally-asymmetric punctum, which polarizes away from the BF in BBs having achieved the rotational polarity to probably fix the BF-AO relationship. Consistently, *Ccdc57*-deficient ependymal multicilia lack the BF-AO coupling and display directional beats at only single cell level. *Ccdc57*$^{-/-}$ tracheal multicilia also fail to fully align their BFs. Furthermore, *Ccdc57*$^{-/-}$ mice manifest severe hydrocephalus, due to impaired cerebrospinal fluid flow, and high mortality. These findings unravel mechanisms governing the planar polarity of epithelial motile cilia.

Motile cilia usually consist of an axoneme of nine symmetrical doublet microtubules (DMTs) assembled from the basal body (BB) and a central pair (CP) of MTs ("9 + 2"). The central MTs are respectively coated with distinct proteinous projections to form the CP apparatus, which contacts with radial spokes protruded from the DMTs to enable the back-and-forth ciliary beat powered by axonemal dynein motors (refer to Fig. 1a for illustrations)[1]. The ciliary beat cycle typically consists of an effective stroke and a recovery stroke[2,3]. The beat direction (the direction of effective strokes) in most organisms studied coincides with the AO, which is perpendicular to the CP plane and points from DMT 1 to the gap between DMTs 5 and 6 (Fig. 1a)[3–8]. Studies on gill multicilia of a fresh-water mussel reveal that their beat directions also coincide with the BF orientation[7]. Subsequently, the BF-indicated BB polarity is commonly used to refer to the beat direction of epithelial cilia[9–11]. For motile cilia with BFs spanning three triplet MTs, such as mammalian cilia[8,12,13], the BB polarity should slightly deviate from the AO (Fig. 1a)[8].

Epithelia that line the walls of mammalian brain ventricles, trachea, and oviduct are abundant in multicilia[11,14]. The most striking feature of "9 + 2"-type motile cilia is their coordinated directional beats across entire tissues, a type of planar cell polarity (PCP) underlying their physiological functions, such as directional cerebrospinal fluid

[1]Key Laboratory of Multi-Cell Systems, Shanghai Institute of Biochemistry and Cell Biology, Center for Excellence in Molecular Cell Science, Chinese Academy of Sciences, Shanghai, China. [2]School of Life Science and Technology, ShanghaiTech University, Shanghai, China. [3]University of Chinese Academy of Sciences, Beijing, China. [4]Center for Biological Imaging, Institute of Biophysics, Chinese Academy of Sciences, Beijing, China. [5]Ministry of Education-Shanghai Key Laboratory of Children's Environmental Health, Institute of Early Life Health, Xinhua Hospital, Shanghai Jiao Tong University School of Medicine, Shanghai, China. [6]Key Laboratory of Systems Health Science of Zhejiang Province, School of Life Science, Hangzhou Institute for Advanced Study, University of Chinese Academy of Sciences, Hangzhou, China. [7]These authors contributed equally: Xinwen Pan, Chuyu Fang, Chuan Shen.
✉e-mail: yanx@shsmu.edu.cn; xlzhu@sibcb.ac.cn

https://doi.org/10.1038/s41467-024-54766-1

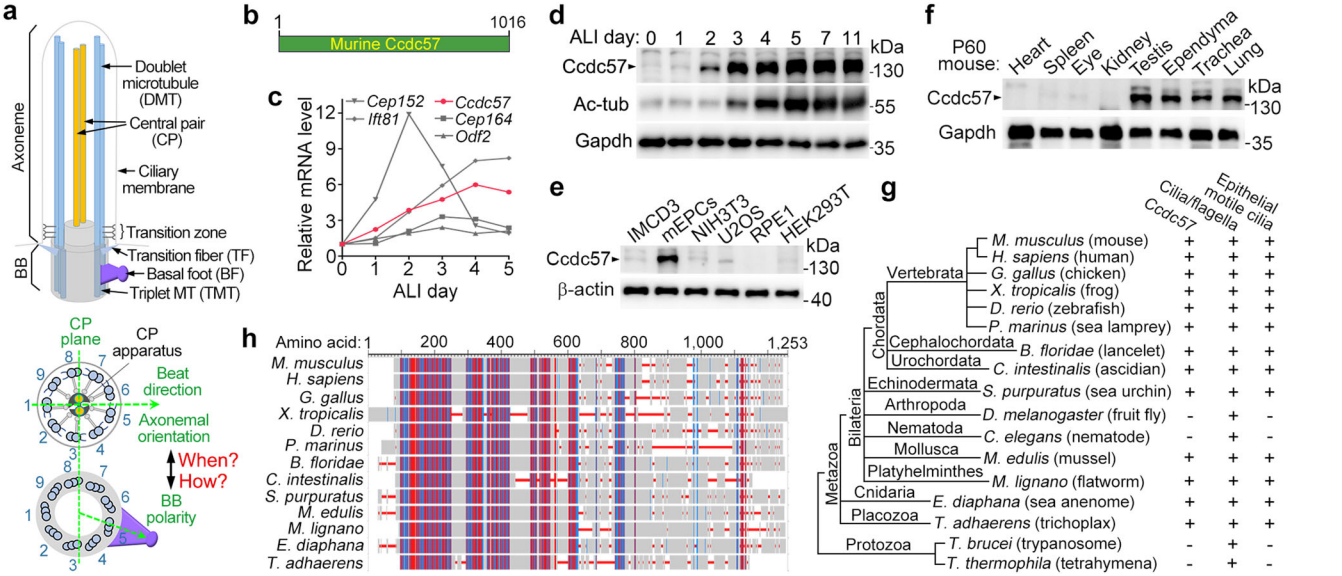

Fig. 1 | *Ccdc57* is implicated in a role in epithelial motile cilia. a Structural features of a "9 + 2" motile cilium. Only two representative DMTs are illustrated in the top panel. The bottom panel illustrates typical transverse top views of the axoneme and the BB. Although the AO has been shown to couple with the BB polarity[7], when and how the coupling occurs are still outstanding questions. **b** A schematic of murine Ccdc57. **c**–**e** Ccdc57 was highly expressed in multiciliated cells. Gene expression profiles (**e**) were from previous cDNA microarray results on mouse tracheal epithelial cells (mTECs) cultured at an air-liquid interface (ALI) for the indicated days[64]. Genes critical for the BB amplification (*Cep152*), BB maturation (*Cep164* and *Odf2*), or cilia formation (*Ift81*)[33,65] are listed for comparisons. In immunoblotting results, Gapdh (**d**) and β-actin (**e**) served as loading control, whereas acetylated tubulin (Ac-tub) (**d**) was a cilia marker. Multiciliated mEPCs (**e**) were cultured to day 15 post serum starvation. One experiment (**d**) and two biologically independent experiments (**e**, **f**) were performed with images from the same experiment presented. **f** Ccdc57 was highly expressed in tissues abundant in multicilia (ependyma, trachea, and lung) or flagella (testis). **g** The presence of *Ccdc57* was correlated with epithelial motile cilia in the evolution. Refer to the Method section for details. **h** Conservation among different Ccdc57 orthologues. Highly conserved and less conserved regions or residues are colored in red and blue, respectively. Source data are provided as a Source Data file.

(CSF) flow, mucous clearance, and ovum transport[9,14]. Notably, ependymal multicilia generally feature two types of PCP: translational polarity, referring to the clustering of BB patches close to one side of cell borders, and rotational polarity, referring primarily to the uniform BB polarities both in individual cells and across the tissue. The Wnt/PCP signaling pathway is essential to both types of the PCP[9,10,15–17]. Both intrinsic (e.g., PCP signaling) and extrinsic (e.g., hydrodynamic forces) cues are thought to modulate cellular cytoskeletal networks so that they reorient BB polarities by pulling on BF tips to facilitate the rotational polarity[9–11,13,18,19]. Defects in this process commonly result in hydrocephalus in mice due to impaired CSF flows[9,16,17,20,21].

How the cilia manage to couple the AO with the BB polarity, however, is completely unknown. Given that normal axonemes and BFs can be assembled independently of each other[21,22], we reasoned that AOs and BB polarities would initially be unrelated and then become coupled through an unknown mechanism during the PCP establishment. In this study, we confirmed the speculation and demonstrated that the rotational polarization of axonemes precedes that of BB polarities in individual mEPCs. Furthermore, we identified Ccdc57 as an evolutionarily conserved BB protein essential for the BF-AO coupling.

Results

Ccdc57 is implicated in a motile cilia-related function in epithelial tissues

We have previously shown that some centriolar and ciliary components are concentrated in fibrogranular materials (FGMs) for proper assemblies into multicilia[23]. To identify novel components involved in the PCP of epithelial motile cilia (Fig. 1a), we re-analyzed our candidate FGM proteins[23] and were interested in a poorly characterized protein Ccdc57 (Fig. 1b). Firstly, both the mRNA and protein levels of *Ccdc57* were highly correlated with motile cilia in both cells and tissues (Fig. 1c–f). Secondly, although CCDC57 is reported as a multifunctional protein for centriole duplication, mitosis, and ciliogenesis[24], our evolution analysis suggested that the presence of *Ccdc57* was correlated with epithelial motile cilia, rather than the cell cycle and ciliogenesis, or even ciliary motility (Fig. 1g). For instance, representative metazoan species containing epithelial motile cilia commonly possessed *Ccdc57* (Fig. 1g, h), including *Trichoplax*, the simplest species of all animals that move through the beating of epithelial monocilium[25,26]. In contrast, *Ccdc57* was absent in nematodes and fruit flies, whose cells undergo centriole duplication and cell cycle. Moreover, nematodes contain only neuronal sensory cilia[27], whereas fruit flies only have sensory cilia and sperm flagella[28]. Nor was *Ccdc57* present in *Trypanosoma* and *Tetrahymena* (Fig. 1g), protozoa with motile cilia or multicilia[29]. We thus speculated that Ccdc57 might have a conserved role in epithelial motile cilia.

Ccdc57 is an FGM component and also localizes as a punctum at the BB distal end in mEPCs

We next examined the subcellular localization of Ccdc57 in mEPCs cultured to day 4 post serum starvation (Fig. 2a), a time when the cells undergoing massive BB biogenesis and ciliogenesis are both present[30,31]. Cep152, Centrin, and Odf2 were used as markers: Cep152 labels entire deuterosomes in early stages (e.g., stage II) of the BB biogenesis and then emerges as a punctum on the proximal wall of mature BBs[31,32]; Centrin marks the distal lumen of BBs or centrioles and also the CP-foot, a rod-like substructure in the ciliary central lumen of multicilia[23]; Odf2 localizes at centriole/BB distal end as a ring and also at the base of the BF[21,33]. Three-dimensional structured illumination microscopy (3D-SIM) revealed that Ccdc57 displayed typical FGM localization patterns, i.e., numerous puncta arrayed into a shape reminiscent of the nucleus (due to their associations with the nuclear envelope surface) in addition to their enrichments in nascent BB-abundant areas in mEPCs (Fig. 2b)[23].

We also noticed that a Ccdc57-positive punctum appeared to be associated with nascent BBs (Fig. 2b)[31,32]. We examined 3D-SIM images

https://doi.org/10.1038/s41467-024-54766-1

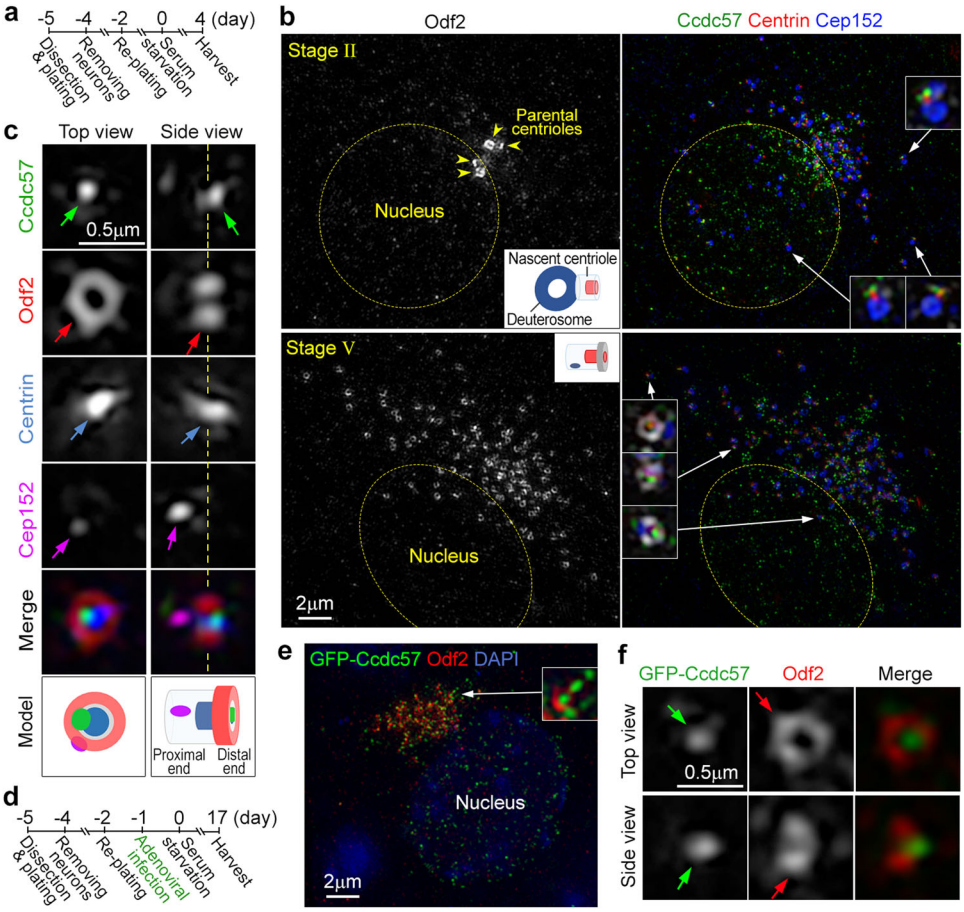

Fig. 2 | Ccdc57 is an FGM component located at the BB distal end as a punctum in mEPCs. a, **b** Localization of Ccdc57 in mEPCs undergoing massive BB biogenesis. Cultured mEPC precursors from P0 mouse brain tissues were induced to differentiate into multiciliated cells through serum starvation as illustrated (**a**)[23]. The cells were immunostained and imaged through 3D-SIM (**b**). Illustrations (side views) (**b**) are provided to aid comprehension of the localizations of Cep152 (blue), Centrin (red), and Odf2 (gray). Dashed circles mark outlines of nuclear envelope-associated Ccdc57 puncta. Representative nascent BBs (transverse images) were magnified 4-fold and are shown as 4-channel-merged images. Note that nascent BBs in stage II are negative for Odf2[23]. **c** Ccdc57 localized at BB distal end as a punctum. Colored arrows point to the BB-localized proteins. Models are provided to aid comprehension. The dashed line marks the middle position of the Odf2-ring. Refer to Supplementary Fig. 1a for the cell image from which the representative BBs were cropped and also for additional examples. **d**–**f** GFP-Ccdc57 recapitulated the FGM and BB localizations of endogenous Ccdc57. mEPCs infected with adenovirus to expressed GFP-Ccdc57 (**d**) were immunostained to visualize Odf2 (**e**, **f**). DAPI, a DNA-specific dye, was used to label the nucleus (**e**). BBs pointed by the white arrow (**e**) were magnified 4-fold to show details. Refer to Supplementary Fig. 1b for an additional mEPC and Supplementary Fig. 1c for the cell image from which the representative BBs (**f**) were cropped and also for additional BB examples. At least three biologically independent experiments were performed (**b**, **c**, **e**, **f**). Source data are provided as a Source Data file.

containing less FGM puncta in BB-enriched regions to avoid their interference and clearly observed the punctum at BB distal end (Fig. 2c and Supplementary Fig. 1a). Interestingly, in transverse BB images (top views), it appeared to localize slightly off the BB axial center, when referring to the ring-shaped Odf2 and the punctate Centrin distributions (Fig. 2c and Supplementary Fig. 1a). In longitudinal BB images (side views), it was positioned slightly distal to the Odf2 ring (Fig. 2c and Supplementary Fig. 1a).

To understand whether the BB and FGM localizations of Ccdc57 persisted in mEPCs with fully-grown multicilia, we expressed GFP-Ccdc57 in mEPCs through adenoviral infection and fixed the cells at day 17 (Fig. 2d). Consistently, GFP-Ccdc57 appeared as numerous puncta associated with the nucleus and BBs (Fig. 2e and Supplementary Fig. 1b). Furthermore, in images with less interference from the FGM puncta, GFP-Ccdc57 was clearly observed as a punctum at the distal end of BBs, slightly distal to the Odf2 ring (Fig. 2f and Supplementary Fig. 1c). Therefore, in sharp contrast to the reported ring-shaped CCDC57 localization at centriolar proximal end in human U2OS cells[24], Ccdc57 localizes at BB distal end as a punctum in mEPCs. As FGMs serve as cellular storages for some BB and ciliary components to prevent them from premature or excessive assembly into nascent BBs or multicilia[23], the concentration of Ccdc57 in FGMs may ensure its timely assembly into nascent BBs.

The Ccdc57 punctum breaks the rotational symmetry of BBs

As eccentrically localized Ccdc57 would break the rotational symmetry of BBs and suggest a role in the PCP of epithelial multicilia, we further verified this. As γ-tubulin localizes both in the BB lumen (Supplementary Fig. 2a)[34] and at BF tip[12,16], we used it as a marker to assess detailed BB localization of Ccdc57 and its possible relationship with the BF, which also breaks the rotational symmetry of BBs. In contrast to previous report[15], we noted that BFs in most mEPCs oriented irregularly even when the cells were cultured to day 20 (Supplementary Fig. 2b). We quantified the extent of the rotational polarity of BBs by considering each arrow marking the BB polarity as a unit vector and measuring the mean vector length of BB patches in individual cells[19]. As a BB patch with full or no rotational polarity should have a mean vector length of 1 or 0, respectively, the collective results (0.30 ± 0.15 at day 10 and 0.29 ± 0.17 at day 20) (Supplementary Fig. 2c) indicated a poor rotational polarity of BBs in individual cells.

https://doi.org/10.1038/s41467-024-54766-1

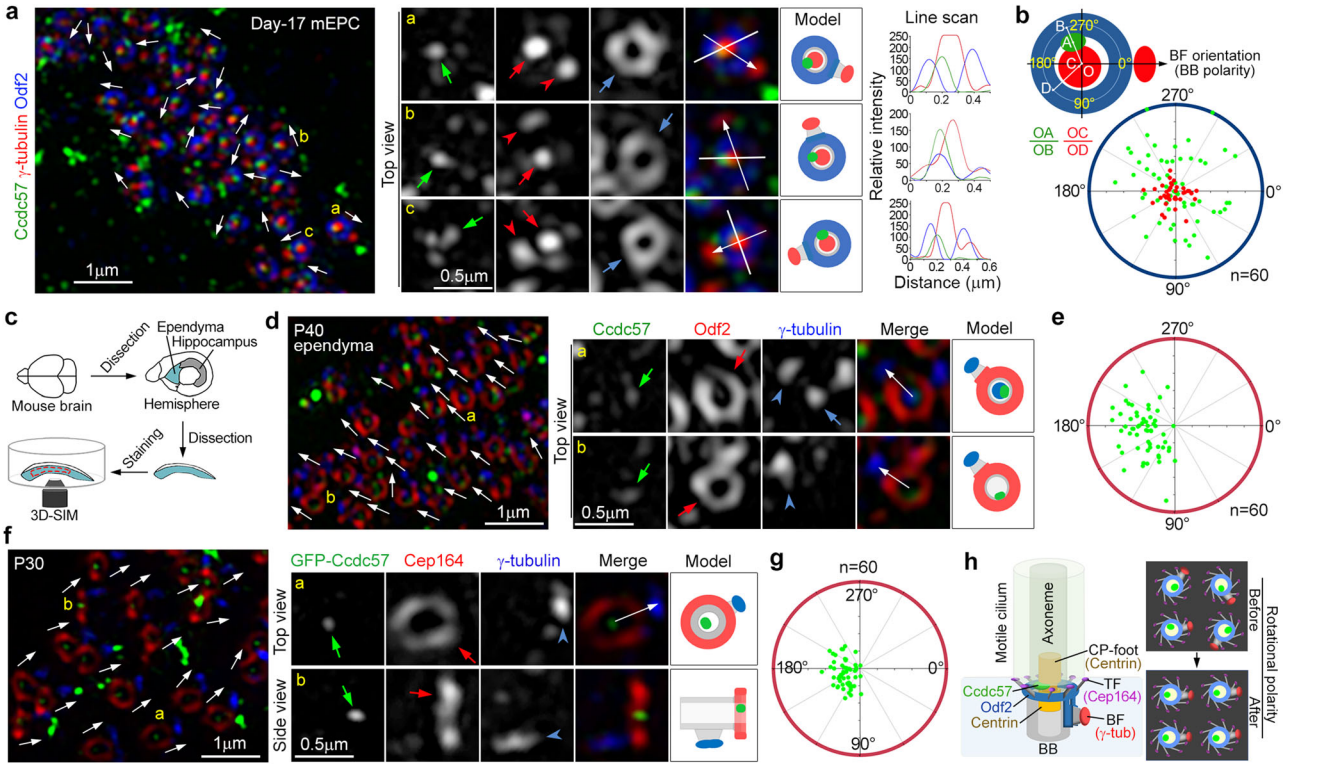

Fig. 3 | Ccdc57 marks a rotationally asymmetric substructure in the BB distal lumen that translocates in rotationally polarized BBs. White arrows indicate the polarities of their adjacent or overlaid (insets) BBs. In insets, colored arrows point to BB localizations of the color-coded proteins, while arrowheads indicate γ-tubulin at the BF tip. **a**, **b** Localization of Ccdc57 in cultured mEPCs. Representative BBs were magnified by 2-fold to show details (**a**). Illustrations are provided to aid comprehension. Line intensity profiles were generated along the white lines. The radar chart (**b**) shows luminal distributions of Ccdc57 and γ-tubulin puncta relative to the Odf2 ring and the BB polarity, measured from 60 transverse BBs. 24 γ-tubulin puncta were located at the center as one spot. **c** Experimental scheme showing dissection of ependymal tissues from mouse brains for 3D-SIM. The region of interest is enclosed by red dashed lines. This is also the region of interest in other experiments. **d**, **e** Ccdc57 localized opposite to the BF in rotationally polarized BBs. Pseudo-colors (**d**) different from those in (**a**) are used to highlight Ccdc57 and Odf2 relationships. The radar chart (**e**) shows the positions of Ccdc57 puncta measured from 60 transverse BBs. Refer to Supplementary Fig. 2 g for BBs in the entire cell and for additional examples. **f**, **g** Localization of GFP-Ccdc57 in rotationally polarized BBs. P30 ependymal tissues were infected with adenovirus and cultured ex vivo for 24 h to express GFP-Ccdc57, followed by immunostaining (**f**). The radar chart (**g**) shows puncta positions of GFP-Ccdc57 measured from 60 transverse BBs. Refer to Supplementary Fig. 2 h for the entire cell and for additional examples. **h** Summarizing models. The left panel illustrates the localization of Ccdc57 relative to other proteins or substructures in a BB. The right panel depicts the translocation of the Ccdc57 punctum (green). TF, transition fiber. At least three biologically independent experiments were performed (**a**, **d**, **f**). Source data are provided as a Source Data file.

To ascertain that different fluorescent channels were well-aligned in 3D-SIM, we routinely visualized deuterosomes by immunostaining Deup1 simultaneously with Alexa Fluor-488, Cy3, and Alexa Fluor-647 to calibrate the microscope prior to imaging for experimental samples (Supplementary Fig. 2d)[32]. We examined day-17 mEPCs and observed that, in transverse BB images, the Ccdc57 punctum was positioned between the Odf2 ring and the luminal γ-tubulin punctum but lacked a fixed positional correlation with the BF (Fig. 3a). Consistently, when the puncta positions relative to the Odf2 ring and the BB polarity were measured from 60 transverse BBs and projected into a radar chart, the Ccdc57 puncta spanned 360° and were apparently more peripheral than the luminal γ-tubulin puncta (Fig. 3b). Therefore, Ccdc57 appears to mark a previously unknown substructure in BB distal lumen that is located in a rotationally asymmetric manner.

The Ccdc57 punctum is located away from the BF in rotationally polarized BBs

The intriguing localization of Ccdc57 prompted us to ask whether its lack of a positional correlation with the BF (Fig. 3a, b) was due to the lack of rotational polarity of BBs in cultured mEPCs (Supplementary Fig. 2b, c). To clarify this, we dissected ependymal tissues from P10, P20, or P30 mice (Fig. 3c). In sharp contrast to cultured mEPCs (Supplementary Fig. 2b), BB patches in the tissues were increasingly organized during the development, e.g., with more BBs aligned in rows (Supplementary Fig. 2e). BB polarities also became increasingly uniform, with the mean vector length being 0.41 ± 0.23, 0.90 ± 0.11, and 0.95 ± 0.05, respectively (Supplementary Fig. 2e, f), consistent with the timing (> P21) of the planar polarity of ependymal multicilia[9,15].

We thus examined the localization of Ccdc57 in > P21 ependymal tissues and observed that the Ccdc57 punctum was now positioned away from the BF inside the Odf2 ring (Fig. 3d, e and Supplementary Fig. 2g). Similar results were obtained when the tissues were infected with adenovirus for 24 h to express GFP-Ccdc57 (Fig. 3f, g and Supplementary Fig. 2h). Therefore, the Ccdc57 punctum displays a polarized localization relative to the BB polarity in rotationally polarized BBs.

Taken together, these results suggest that the rotational polarization of motile cilia also involves the translocation of the Ccdc57 punctum from an indefinite position to a polarized position away from the BF (Fig. 3h).

Ccdc57-deficient mice manifest hydrocephalus, high mortality, and kyphosis

To discern Ccdc57's function, we obtained *Ccdc57* knockout-first (Kof) (*Ccdc57*$^{Kof/Kof}$) mice (Fig. 4a) and found that they appeared to be morphologically normal. We suspected that the *Kof* cassette might not completely inactivate *Ccdc57*, similar to our previous case[35], and thus crossed the mice with *EIIa-Cre* mice[36] to generate *Ccdc57* knockout (*Ccdc57*$^{-/-}$) mice (Fig. 4a, b).

https://doi.org/10.1038/s41467-024-54766-1

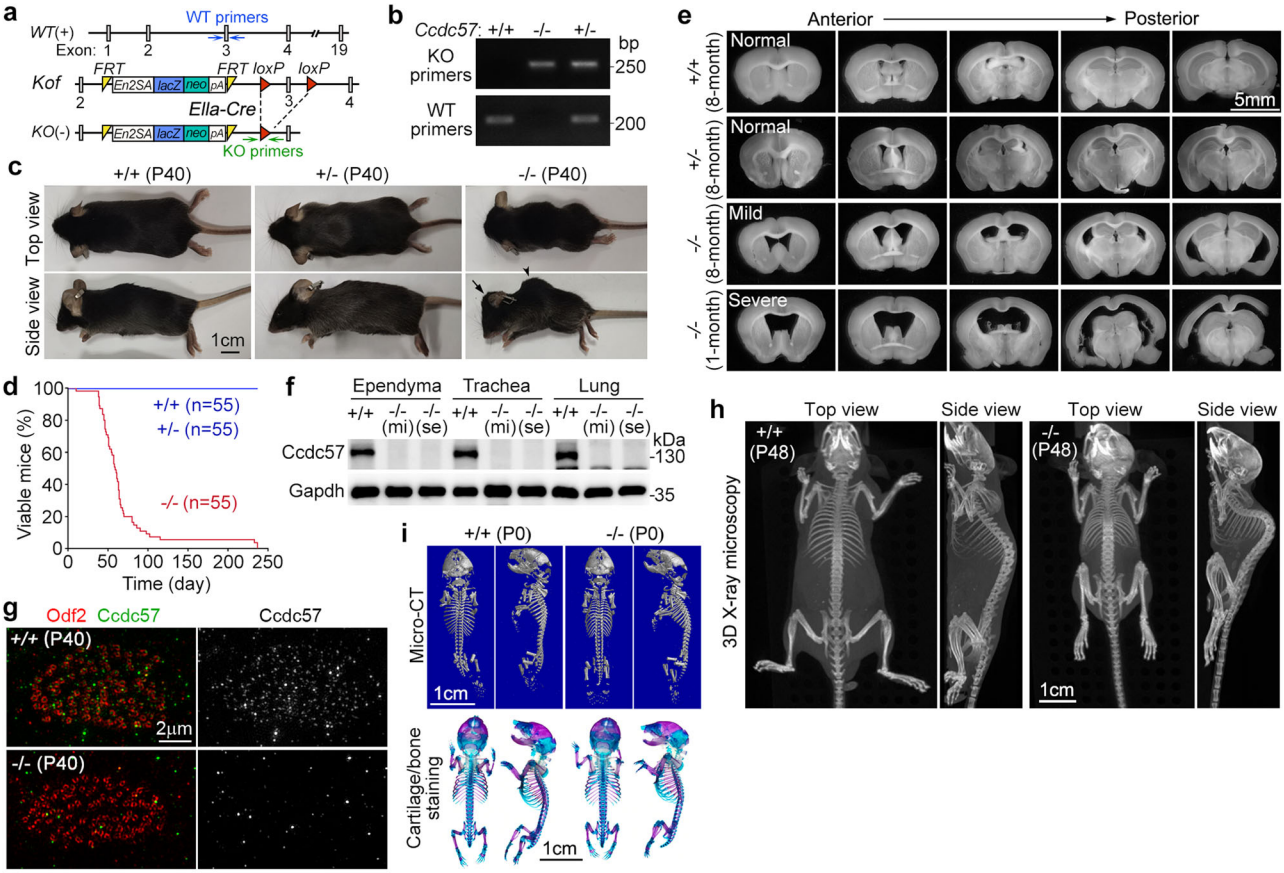

Fig. 4 | *Ccdc57*-deficient mice tend to develop severe hydrocephalus and kyphosis. a Illustrations for *Ccdc57* knockout (KO) strategy. The knockout-first (Kof) allele contains a trapping cassette flanked by two flippase-recognition target (*FRT*) sites. The KO allele was generated by using *Ella-Cre* mice. *En2SA*, En2 splice acceptor; *LacZ*, β-galactosidase gene; *neo*, neomycin-resistant gene; *pA*, poly-adenylation signal. Arrow pairs indicate PCR primers for genotyping. **b** Representative genotyping results from three P0 littermates. **c** Typical dome-shaped skull (arrow) and kyphosis (arrowhead) of *Ccdc57*$^{-/-}$ mice. **d** Survival rates of mice. **e** Representative 250 μm-thick coronal sections. *Ccdc57*$^{-/-}$ mice with longer life span always showed moderately enlarged ventricles. **f** Complete depletion of Ccdc57 in *Ccdc57*$^{-/-}$ multicilia-abundant tissues. Tissue lysates from a P30 wild-type mouse, a P30 *Ccdc57*$^{-/-}$ littermate with severe (se) hydrocephalus, and a P100 *Ccdc57*$^{-/-}$ mouse with mild (mi) hydrocephalus were used for the immunoblotting. Gapdh served as a loading control. **g** *Ccdc57* deficiency abolished immunofluorescent signals of Ccdc57 in E1 cells. Ependymal tissues from the indicated littermates were co-immunostained to visualize Ccdc57 and Odf2 (BB marker). Note that only some non-specific background puncta remained in the representative *Ccdc57*$^{-/-}$ cell. Refer to Supplementary Fig. 3a, b for immunoblotting and immunostaining results of cultured mEPCs. **h** *Ccdc57*$^{-/-}$ mice displayed over-curvature of the spine. Images were cropped from whole-body scans (Supplementary Movies 1, 2). **i** Skeletons of representative neonatal mice. Skeletons of two pairs of P0 wild-type and *Ccdc57*$^{-/-}$ littermates were visualized through micro-computed tomography (micro-CT), followed by staining with Alcian blue and Alizarin red to visualize cartilages (blue) and bones (red)[66]. Two biologically independent experiments were performed (**f**, **g**). Source data are provided as a Source Data file.

Neonatal *Ccdc57*$^{-/-}$ mice were born normally in both morphology and viability at roughly the predicted Mendelian ratio (23%; total $n = 188$), indicating that Ccdc57 is dispensable for embryonic development. The male mice appeared to be sterile and *Ccdc57*$^{-/-}$ female mice were fertile in the mating test. Importantly, the majority of them developed a dome-shaped skull that became more and more prominent from about 3 weeks after birth (Fig. 4c). Approximately half of them died by 2-month-old and 90% died before 3-month-old (Fig. 4d). Heterozygotic (*Ccdc57*$^{+/-}$) mice were morphologically indistinguishable from their wild-type littermates and displayed normal life span (Fig. 4c, d). All the *Ccdc57*$^{-/-}$ mice examined ($n = 43$; ≥ P21), including those with a normal skull appearance, displayed enlarged ventricles of varying extent as compared to their wild-type ($n = 55$) littermates (Fig. 4e). *Ccdc57*$^{-/-}$ mice with a dome-shaped skull always displayed heavily enlarged ventricles, or severe hydrocephalus, when dissected (Fig. 4e), and the mortality of *Ccdc57*$^{-/-}$ mice appeared to be correlated with the severity of hydrocephalus. Ventricles of *Ccdc57*$^{+/-}$ mice ($n = 90$), however, were similar to those of their wild-type littermates in morphology (Fig. 4e). Immunoblotting and immunostaining confirmed the complete depletion of Ccdc57, regardless of the severity of hydrocephalus (Fig. 4f, g and Supplementary Fig. 3a, b). Therefore, *Ccdc57* deficiency results in hydrocephalus, a phenotype frequently associated with defective ependymal multicilia[14,37,38] and observed in *ccdc57*-deficient zebrafish as well[39].

Ccdc57$^{-/-}$ mice with a dome-shaped skull also exhibited obvious kyphosis (Fig. 4c), whereas those with a normal-shaped skull (including those before the emergence of a dome-shaped skull) did not. This kyphosis phenotype was confirmed to be an over-curvature of the spine when their skeletons ($n = 9$) were compared with those of their wild-type littermates ($n = 4$) (Fig. 4h and Supplementary Movies 1, 2). When neonatal mice were examined, skeletons of the *Ccdc57*$^{-/-}$ mice ($n = 4$) and their wild-type littermates ($n = 4$) indeed did not show obvious morphological differences (Fig. 4i). Neither did they show obvious developmental differences in cartilages and bones (Fig. 4i). Therefore, the kyphosis is probably associated with the development of severe hydrocephalus.

Ccdc57 deficiency disrupts directional ciliary beat across ependymal tissues but not within individual cells

We next examined *Ccdc57*$^{-/-}$ ependymal multicilia for defects. As scanning electron microscopy (EM) did not suggest defects in ciliary

https://doi.org/10.1038/s41467-024-54766-1

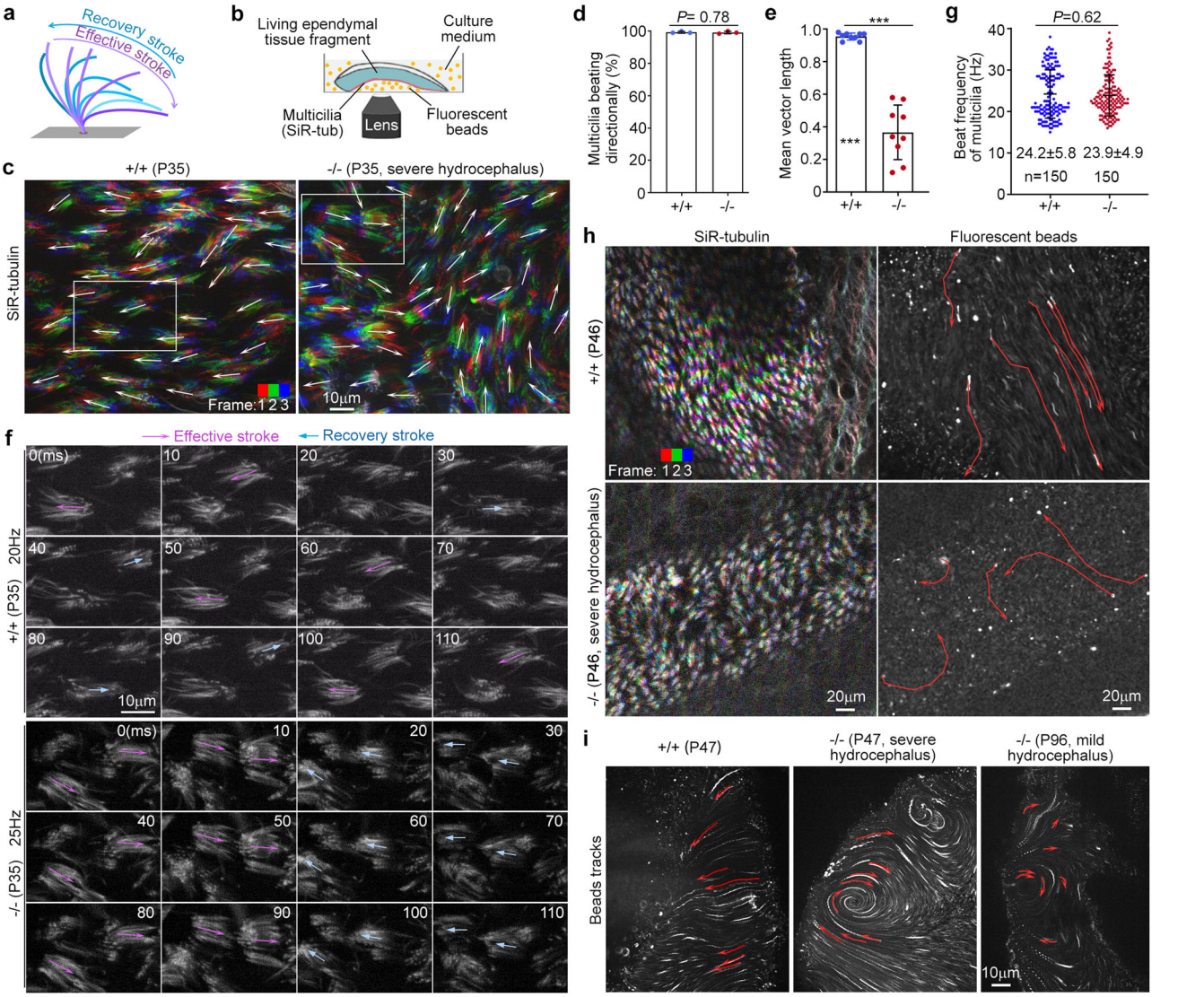

Fig. 5 | *Ccdc57* deficiency impairs tissue-level, but not cell-level, directional ciliary beats. Quantification results in (**d**, **e**, and **g**) are presented as mean ± SD plus sample dots. *P*-values were from unpaired two-tailed student's *t*-test. *** $P < 0.001$. **a** Illustration for the beat pattern of an ependymal cilium (side views). **b** Experimental setup. Cilia motilities were imaged with a spinning disk confocal microscope for SiR-tubulin-labeled cilia alone (**c**) or together with fluorescent beads that served as tracers of liquid flows (**h**, **i**). Note that cilia recorded in this way are mostly top views. **c** Beat directions of multicilia (arrows) in individual E1 cells of representative microscopic fields. Images were acquired at 10 ms intervals on ependymal tissues from P35 littermates. The first three consecutive frames, cropped from Supplementary Movies 3 and 4, were pseudo-colored and merged to show ciliary motilities. Representative fields from other littermates are presented in Supplementary Fig. 3d. **d** Percentages of multicilia displaying directional beats, quantified from three mice of each genotype described in (**c**). 200 multiciliary bundles were scored per mouse. **e** Quantification of mean vector length from 9 microscopic fields from three mice of each genotype described in (**c**). $P = 4.7 \times 10^{-6}$. The mean vector length is 1 when all multiciliary bundles in a field beat in the same direction or 0 when randomly. **f** Image sequences showing directional ciliary beat in individual *Ccdc57*$^{-/-}$ E1 cells, cropped from Supplementary Movies 3 and 4 to cover three beat cycles. Effective and recovery strokes are indicated by colored arrows. Refer to Supplementary Fig. 3c, d for additional examples. **g** *Ccdc57* deficiency did not alter multicilia beat frequencies. Quantification from three mice per genotype (50 multiciliary bundles per mouse) was pooled. **h**, **i** *Ccdc57* deficiency impaired multicilia-driven liquid flows. The first three consecutive frames cropped from Supplementary Movies 5 and 6 were merged to show ciliary distributions and motilities. The first corresponding frames of beads were superimposed with trajectories of traceable, rapidly moving beads in the first 858 ms to show flow directions (**h**). In (**i**), all frames of beads were projected together to show flow patterns. Trajectories of traceable, rapidly moving beads in the first 300 ms (P47) or 400 ms (P96) were superimposed to show flow directions. Source data are provided as a Source Data file.

number and morphology (Supplementary Fig. 3c), we investigated ciliary motilities (Fig. 5a)[2]. As severe hydrocephalus could exert deleterious influences on cilia, we examined mice with mild and severe hydrocephalus in order to focus on common features.

As ependymal multicilia beat directionally tissue-wide after P21[9,15,22], we examined living ependymal tissues from two pairs of P35 littermates in which the *Ccdc57*$^{-/-}$ mice displayed severe hydrocephalus and one pair of P50 littermates with the *Ccdc57*$^{-/-}$ mouse showing mild hydrocephalus. As the tissues were opaque, we sought to use fluorescent microscopy and found that staining with SiR-tubulin, an MT-specific fluorescent dye[40], enabled high-contrast live imaging of ciliary beats through high-speed spinning-disk confocal microscopy (Fig. 5b, c). In the wild-type samples, multicilia beat in a back-and-forth manner grossly towards one direction at both cell and tissue levels (Fig. 5c, Supplementary Fig. 3d–f,and Supplementary Movie 3). In the *Ccdc57*$^{-/-}$ samples, multicilia within single cells still beat rhythmically toward one direction (Fig. 5c, d, Supplementary Fig. 3d–f and Supplementary Movie 4). The beat direction of different E1 cells in the

same tissue, however, differed markedly, regardless of the severity of hydrocephalus phenotypes (Fig. 5c, e and Supplementary Fig. 3d). The multiciliary beat frequencies were usually similar among neighboring cells but could vary largely among cells from different tissue fragments (Fig. 5f, g and Supplementary Fig. 3e, f)[41,42]. Despite this, the beat frequencies were not grossly altered by the *Ccdc57* deficiency (Fig. 5g).

We next examined cilia-driven liquid flows by imaging motilities of 250 nm fluorescent latex beads suspended in a culture medium (Fig. 5b)[22,38]. Fresh ependymal tissues from three wild-type mice and three *Ccdc57*$^{-/-}$ littermates, one with mild and two with severe hydrocephalus, were assayed. Underneath the wild-type tissues, unidirectional liquid flows were observed in areas abundant in beating multicilia (Fig. 5h, i and Supplementary Movie 5). In contrast, the irregular ciliary beats of the *Ccdc57*$^{-/-}$ tissues only resulted in oscillations or regional whirling of the beads (Fig. 5h, i and Supplementary Movie 6). Consistently, *ccdc57*-deficient zebrafish display disorganized ependymal multiciliary beats and abnormal CSF flow[39,43]. Therefore, Ccdc57 has a conserved role in the PCP of multiciliary beats in the ependyma.

BBs fail to establish the rotational polarity in *Ccdc57*-deficient ependymal tissues

Epithelial motile cilia are generally believed to beat towards the BF[9]. In this context, the unidirectional beat of multicilia in individual *Ccdc57*$^{-/-}$ cells (Fig. 5) would suggest a normal rotational polarity of BBs in individual E1 cells but different directions of the polarity across the tissue. To testify this, we labeled BBs with Cep164 and BFs with γ-tubulin or Centriolin (Fig. 6a, b and Supplementary Fig. 4a–c), which localizes at the middle zone of BFs as a ring (Supplementary Fig. 4b)[12]. Surprisingly, in sharp contrast to the grossly uniform BB polarity in wild-type ependymal E1 cells, BBs in individual *Ccdc57*$^{-/-}$ E1 cells were largely disoriented regardless of the severity of hydrocephalus (Fig. 6a–c and Supplementary Fig. 4a, c). We also quantified the BB number per cell and confirmed that *Ccdc57* deficiency did not affect BB biogenesis (Supplementary Fig. 4d).

Transmission EM also indicated that, while BFs of most BBs in wild-type E1 cells were oriented to a similar direction in cross-sections, they were disoriented in *Ccdc57*$^{-/-}$ E1 cells (Fig. 6d). Even neighboring BBs displayed distinct polarities (Fig. 6d). The mean vector length (0.35 ± 0.17) also revealed defective rotational polarity as compared to the wild-type cells (0.96 ± 0.06) (Fig. 6e). By contrast, we did not observe morphological defects in BBs and their BFs. Therefore, quite contradictory to the initial speculation, *Ccdc57* deficiency actually impairs the rotational polarity of BBs in individual E1 cells, indicating that the ciliary beat direction can be decoupled from the BB polarity.

Ccdc57 deficiency neither impairs the translational polarity of BBs nor influences subcellular localizations of core PCP proteins

To clarify whether *Ccdc57* deficiency impacted the translation polarity[9], we labeled cell borders with ZO-1[44] and BBs with Cep164. Relative BB patch areas were similar between E1 cells of wild-type mice and *Ccdc57*$^{-/-}$ mice with mild hydrocephalus but moderately increased in E1 cells of *Ccdc57*$^{-/-}$ mice with severe hydrocephalus (Supplementary Fig. 4e–g), possibly due to deleterious influences of the severe disease. Furthermore, BB patches in *Ccdc57*$^{-/-}$ E1 cells still displayed obvious asymmetric distributions, regardless of the severity of hydrocephalus (Supplementary Fig. 4e, f, h). These results suggest that *Ccdc57* deficiency does not impair the translational polarity.

To clarify whether *Ccdc57* deficiency impacted core PCP proteins, we tested several commercial antibodies but failed to find suitable ones for immunostaining in ependymal tissues except for the anti-Dvl1 antibody, which decorated BBs and some peri-BB puncta similarly in *Ccdc57*$^{-/-}$ and wild-type E1 cells (Supplementary Fig. 4i)[15]. We infected ependymal tissues cultured ex vivo with adenovirus to express Dvl2-GFP or mCherry-Vangl2 at low levels and observed that they displayed asymmetric localizations at a side of E1 cells in both *Ccdc57*$^{+/+}$ and *Ccdc57*$^{-/-}$ tissues (Supplementary Fig. 4j, k). Dvl2-GFP and mCherry-Vangl2 tended to localize close to and away from BB patches, respectively (Supplementary Fig. 4j–l), consistent with their canonical localization patterns[9,10]. Therefore, *Ccdc57* deficiency does not influence subcellular localizations of core PCP components.

Ccdc57 deficiency decouples the BB polarity from the AO

We reasoned that the decoupling of ciliary beat direction from the BB polarity in *Ccdc57*$^{-/-}$ ependymal cells would be due to a decoupling of either the beat direction or the BB polarity from the AO. To assess the first possibility, we examined AOs in EM micrographs containing multiple axonemal cross-sections. We observed that most axonemes in a micrograph are still oriented towards a similar direction in *Ccdc57*$^{-/-}$ ependymal tissues, analogous to those in wild-type tissues (Fig. 6f, g). Therefore, the ciliary beat direction is still coupled with the AO in *Ccdc57*$^{-/-}$ ependymal E1 cells.

To assess the second possibility, we initially examined EM micrographs simultaneously containing cross-sections of both axonemes ($n \geq 3$) and BF-containing BBs ($n \geq 3$). In each of 30 such micrographs from 4 wild-type mice (> P21), the BB polarities and the CP planes were relatively uniform and roughly orthogonal to each other (Supplementary Fig. 5a). By contrast, while the CP planes were relatively uniform in each of 30 micrographs from 3 *Ccdc57*$^{-/-}$ littermates, the BB polarities were markedly disoriented (Supplementary Fig. 5a).

Next, we performed serial-section EM to directly examine the same cilia. We tracked from the axoneme all the way down to the BB over a thickness of > 12 μm and identified 7 wild-type and 6 *Ccdc57*$^{-/-}$ cilia whose AOs and BB polarities were both visible. In the wild-type cilia, the AO and the BB polarity were indeed highly correlated (Fig. 6h, i)[7,8]. In sharp contrast, while *Ccdc57*$^{-/-}$ axonemes in the same micrograph displayed similar orientations, their BB polarities pointed towards strikingly different directions (Fig. 6h, i).

Therefore, Ccdc57 functions to couple the BB polarity with the AO. In individual *Ccdc57*$^{-/-}$ ependymal cells, axonemes are still able to achieve rotational polarity while their BB polarities remain irregular.

The BB polarity is initially decoupled from the AO during mouse development

The rotational polarization of axonemes independently of BB polarities (Figs. 5 and 6) prompted us to investigate whether AOs and BB polarities were initially unrelated in the development. Considering the difficulty of tracking cilia through serial-section EM, we sought to identify an early developmental stage in which a significant portion of E1 cells contained multicilia that beat in diverse directions. Wild-type P4 ependymal cells would be a choice because only 47% of them have been shown to display varying extents of the rotational polarity of BBs[15]. Consistently, we found that multicilia beat directionally in 52% of E1 cells ($n = 191$) at P4, whereas multicilia beat diversely in the remaining 48% of E1 cells (Fig. 7a and Supplementary Movie 7). In comparison, multicilia beat directionally in 94% of E1 cells ($n = 140$) at P20 (Fig. 7a and Supplementary Movie 8). Therefore, mouse P4 ependyma contains multicilia that beat either diversely or directionally.

We thus examined cilia in P4 ependymal tissues using a high throughput EM technique, the automatic collector of ultrathin sections scanning EM (AutoCUTS-SEM) (Fig. 7b)[45], to increase the efficiency. Indeed, microscopic fields containing cilia of diverse AOs were observed (Fig. 7c, d). Of 41 successfully tracked cilia, many had unusual BB polarities relative to AOs (Fig. 7e, fand Supplementary Movie 9): In 61% of them, the included angle between the two directions exceeded ± 20°, i.e., over the average size (19°) of the angle in tracheal cilia[8] and possibly over measuring errors due to minor twists between the cross-section planes of axonemes and BFs. Twenty-three of the 41 cilia were

https://doi.org/10.1038/s41467-024-54766-1

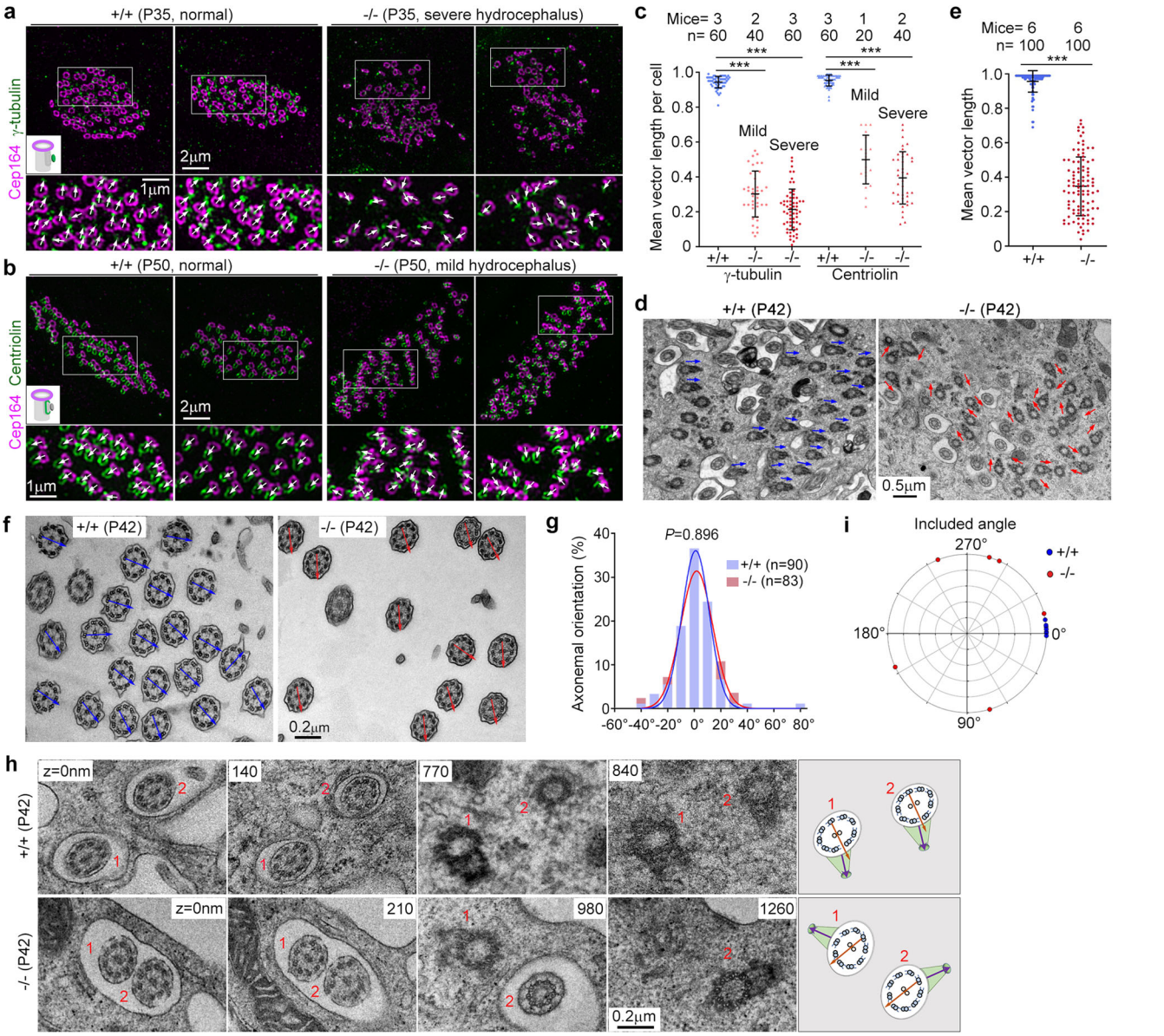

Fig. 6 | *Ccdc57* deficiency decouples the BB polarity from the AO. Quantification results in (**c**, **e**, **g**) are presented as mean ± SD plus sample dots. *P*-values were from unpaired two-tailed student's *t*-test. *** $P < 0.001$. Arrows in micrographs indicate BB polarities (**a**, **b**, **d**) or AOs (**f**). **a**–**c** BBs in *Ccdc57*$^{-/-}$ E1 cells lacked the rotational polarity. Ependymal tissues were immunostained for Cep164 to visualize BBs and γ-tubulin (**a**) or Centriolin (**b**) to visualize BFs. Diagrams (tilted side views) illustrate the protein localizations on the BB. Two neighboring BB patches, cropped from micrographs in Supplementary Fig. 4a and c, are presented for each mouse. Mean vector lengths (mean ± SD plus sample dots) (**c**) were measured from 20 BB patches (cells) for each P35 or P50 mouse. Unpaired two-tailed student's *t* test. γ-tubulin: $P = 2.5 \times 10^{-30}$ for +/+ vs −/− (Mild), $P = 1.1 \times 10^{-53}$ for +/+ vs −/− (Severe); Centriolin: $P = 6.4 \times 10^{-12}$ for +/+ vs −/− (Mild), $P = 2.6 \times 10^{-25}$ for +/+ vs −/− (Severe). Theoretically, BB patches with full or no rotational polarity should have a mean vector length of 1 or 0, respectively. Mild, mild hydrocephalus; Severe, severe hydrocephalus. **d**, **e** Representative transmission EM micrographs (**d**) and quantification results (**e**). Each mean vector length (**e**) was calculated from a full-size EM micrograph, from mice ranging from P21 to P60. 100 full-size EM micrographs from six mice for each genotype. $P = 2.0 \times 10^{-64}$. **f**, **g** *Ccdc57* deficiency did not impact the rotational polarity of axonemes. Representative EM images (**f**) were from the ependymal tissues of littermates. Quantification results (**g**) are presented as distributions of the mean angle of axonemes. 9 full-size EM micrographs from 3 mice ranging from P21 to P60 were quantified for each genotype. Each micrograph contained at least 6 clear axonemal cross-sections. **h**, **i** Decoupled BB polarities from AOs in *Ccdc57*$^{-/-}$ E1 cells. Representative serial sections of 70 nm thickness (**h**) are presented. Illustrations depict the AO and the BB polarity of the cilia. One experiment (**h**) was performed. Radar chart (**i**) shows included angles between the two directions, measured respectively from 7 wild-type and 6 *Ccdc57*$^{-/-}$ cilia. Source data are provided as a Source Data file.

from regions with diverse AOs (Fig. 7e; red dots in Fig. 7f) and thus probably from multicilia of uncoordinated beats (Fig. 7a). 83% of these cilia had an included angle over ± 20° (Fig. 7f). In the remaining 18 cilia from regions with relatively uniform AOs (blue dots in Fig. 7f and Supplementary Fig. 5b) and thus probably from multicilia of coordinated beats (Fig. 7a), 33% had included angles over ± 20° (Fig. 7f), suggesting increased BF-AO coupling in individual cells whose multiciliary bundle had achieved unidirectional beats. Therefore, AOs and BB polarities are initially decoupled and become gradually coupled following mouse development (Fig. 7g).

Ccdc57$^{-/-}$ tracheal multicilia fail to fully align their BFs

Although Ccdc57 was highly expressed in cultured multiciliated mouse tracheal epithelial cells (mTECs) (Fig. 1c, d), we did not observe obvious phenotypes associated with dysfunctions of airway multicilia, such as coughing and sneezing[21], in *Ccdc57*$^{-/-}$ mice. Unlike in the

https://doi.org/10.1038/s41467-024-54766-1

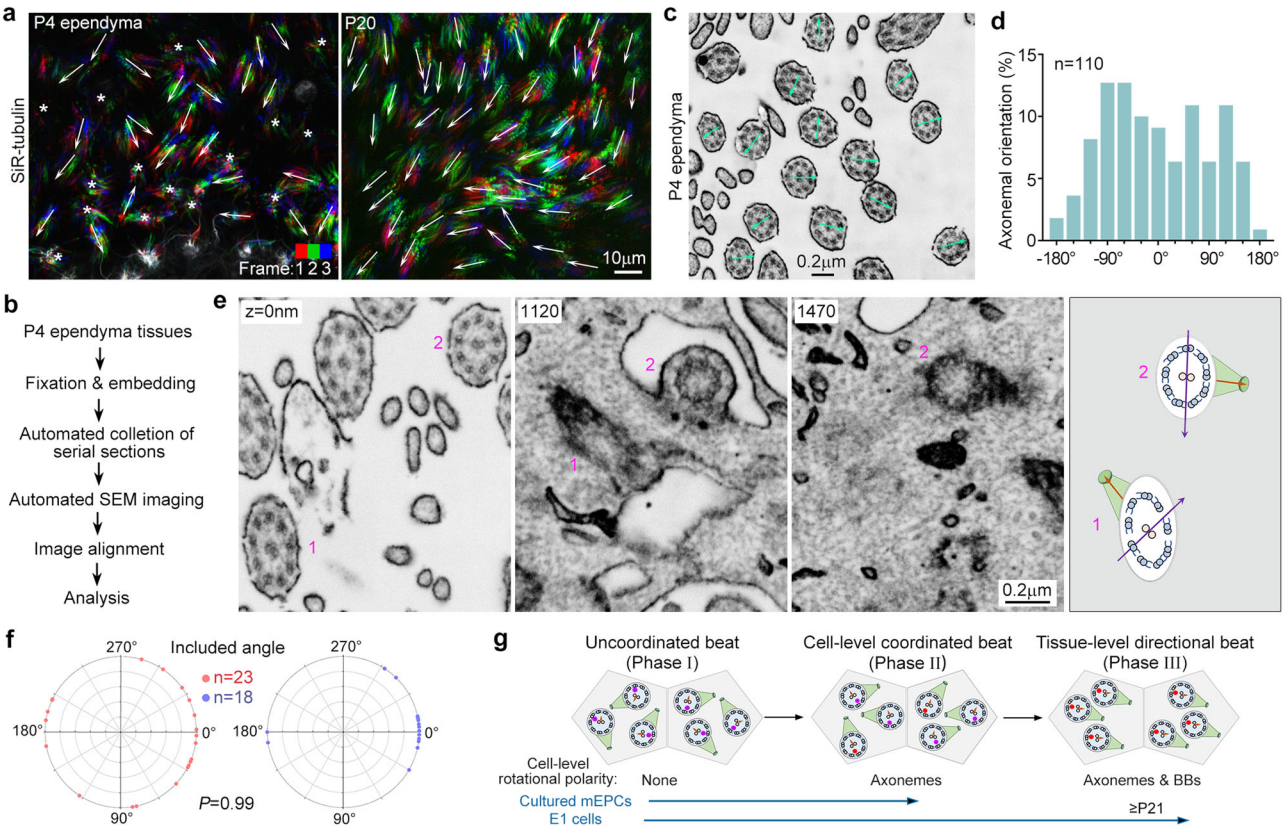

Fig. 7 | BB polarities and AOs are initially decoupled during mouse development. a Wild-type P4 ependymal tissues were abundant in multicilia with uncoordinated beats (asterisks). Ciliary motilities were imaged at 10 ms intervals. The first three consecutive frames were pseudo-colored and merged to show ciliary motilities. Arrows indicate beat directions of multicilia showing coordinated beats. Refer to Supplementary Movies 7 and 8. **b** Workflow for AutoCUTS-SEM. Ependymal samples were fixed, embedded in resin, and serially sectioned using AutoCUTS. Ultrathin sections were adhered to tape and transferred onto a wafer. High-throughput SEM images were acquired[45], especially in regions with diverse AOs. **c**, **d** P4 ependymal cells contained multicilia with diverse AOs. AOs are indicated by arrows in the typical SEM image (**c**), and their distributions (**d**) were quantified from six SEM micrographs, each containing at least 13 clear axonemal cross-sections. **e**, **f** BF-AO relationships in P4 cilia. Two numbered cilia were tracked from axonemes to BFs in representative serial cross-sections from Supplementary Movie 9 (**e**). Radar charts (**f**) show included angles between the AO and BB polarity from 41 cilia in 4 cells. The red and blue dots were from regions with diverse and uniform AOs, respectively. An unpaired two-tailed student's *t*-test was performed. **g** Model for progression of ciliary rotational polarities. Cilia are depicted as top views to show AOs (arrows) and BFs (green). For simplicity, the translational polarity is not depicted. Nascent multicilia initially lack BF-AO coupling and display uncoordinated beat due to randomized AOs (phase I). Axonemes in individual cells gradually unify their AOs to achieve the rotational polarity and coordinated beats (phase II), with some possibly achieving BF-AO coupling. In phase III, BF-AO coupling and rotational polarity of BBs are achieved in both individual and different E1 cells, leading to tissue-level directional beats of multicilia. BB-localized Ccdc57 shifts from a random position relative to the BF (purple spot) in phase I to a position opposite the BF (red spot) in phase III to fix the BF-AO relationship. Cultured mEPCs only reach phase II naturally, whereas E1 cells in the ependyma progress to phase III at around P21. Source data are provided as a Source Data file.

ependyma, BBs in the trachea and oviduct spread densely over the apical cell surface[18,32,46]. Furthermore, they can achieve the rotational polarity autonomously in vitro[18]. In cultured mTECs, nascent BBs with diverse polarities initially gather into many floret-like clusters (Fig. 8a)[18,32]. The BBs are then scattered, and BB polarities become mostly oriented within 180° (Fig. 8a)[18]. Subsequently, the BBs are gradually organized into rows, with their polarities increasingly unified so that BFs are also aligned in rows (Fig. 8a)[18].

To assess the role of Ccdc57 in mTECs, we immunostained the tracheal tissues of two pairs of P40 littermates. Ccdc57-positive puncta were abundant in BB patches of wild-type mTECs, with similar BB localization of Ccdc57 as in mEPCs, and were abolished in *Ccdc57*-deficient mTECs (Fig. 8b). Consistent with previous reports[8,18], both BBs and BFs in individual cells lined nicely in rows (93%; $n = 180$) (Fig. 8a, c), indicative of an "alignment" pattern (Fig. 8a). The remaining 7% displayed a "scatter" pattern (Fig. 8a). In individual *Ccdc57*$^{-/-}$ cells, however, BFs mostly displayed a "scatter" pattern (85%; $n = 181$) even though their BBs were partly organized in rows (Fig. 8c). Although the high densities of BBs (Fig. 8b, c) precluded a quantitative comparison between mean vector lengths of BB polarities in both genotypes, these results still indicate that individual BB patches in *Ccdc57*$^{-/-}$ mTECs fail to achieve full rotational polarity (Fig. 8d).

Finally, we examined multicilia-driven liquid flows in the cavity of tracheal fragments (Fig. 8e). Fluorescent beads below beating cilia moved quickly in similar directions from both genotypes (Fig. 8f). Quantifications indicated that bead velocities were slightly decreased (Fig. 8g), echoing the lack of obvious respiratory phenotypes in *Ccdc57*$^{-/-}$ mice.

Discussion

We demonstrate that the canonical BF-AO relationship (Fig. 1a) requires Ccdc57 to lock the BF-AO relationship (Fig. 7g), probably when the BF is turned to match the AO by cytoskeletons[9,10]. The BB polarity is initially irrelevant to the AO (Fig. 7a–f), and is dispensable for the rotational polarity of axonemes and their beat directions when the BF-AO coupling is not accomplished (Figs. 5, 6, and 7).

We propose a three-phase model for the PCP establishment of ciliary beats (Fig. 7g). In developing ependyma, the initial irregular ciliary beats (Fig. 7a and Supplementary Movie 7) are not related to the BB polarity (Fig. 7g, phase I). This is followed by the cell-level

https://doi.org/10.1038/s41467-024-54766-1

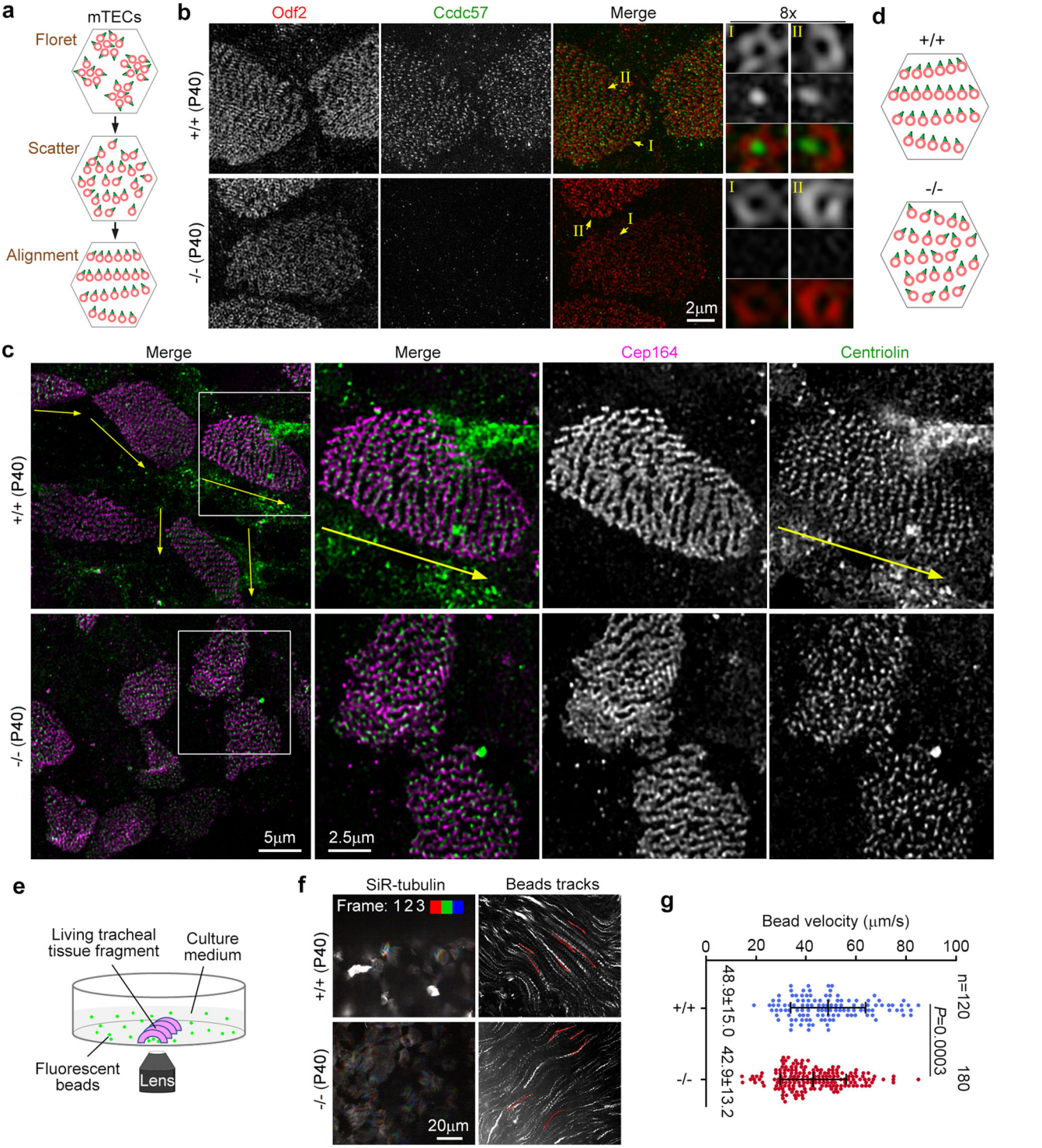

directional beat (Fig. 7a and Supplementary Movie 7), through BF-independent alignments of AOs (Fig. 7g, phase II). From phase II, more and more BFs become coupled with AOs so that cytoskeletons fine-tune AOs through BFs to eventually achieve uniform tissue-level ciliary beats (phase III). Phase II can be achieved in the absence of Ccdc57 in mouse E1 cells (Figs. 5 and 6). mEPCs cultured in vitro can also reach phase II because many achieve directional ciliary beat from around day 7 post serum starvation[15,38,47] but lack uniform BB polarities at even day 20 (Supplementary Fig. 2b, c). Therefore, phase II is most likely accomplished through self-organization, probably via hydrodynamic coupling among neighboring beating cilia[15,48,49]. Nevertheless, proper ciliary/BB structures, extrinsic guidance cues, and interplays among them are all required for epithelial cells to reach phase III. For instance, the PCP signaling provides cross-cell guidance cues essential for phase III[15–17]. In vitro cultured mEPCs are reported to require external hydrodynamic forces to achieve phase III[15]. On the other hand, BBs lacking axonemes fail to achieve the rotational polarity[22], and E1 cells also fail to reach phase III in the absence of the BF-AO coupling (Figs. 5 and 6) or the BF[21], while proper localizations of PCP proteins remain (Supplementary Fig. 4)[21,22]. The lengthy time required for reaching phase III in mouse ependyma (from approximately P4 to P21)[9,15] further signifies the intricacy of the interplays between extrinsic guidance cues and ciliary/BB structures during the progression from phase II to phase III.

Fig. 8 | BFs fail to become fully aligned in *Ccdc57*-deficient tracheal multicilia. **a** Illustrations showing the progression of BB organizations and polarities in differentiating tracheal epithelial cells. **b** Ccdc57 puncta were abolished in *Ccdc57*-deficient mTECs. Tracheal tissues from a pair of littermates were subjected to immunostaining and 3D-SIM. Odf2 served as BB marker. Two representative BBs (arrows) were magnified to show details. **c** Representative confocal micrographs of BB patches. Cep164 and Centriolin served as BB markers and BF markers, respectively. Two biologically independent experiments were performed (**c**). For each BB patch showing an "alignment" pattern, an arrow roughly perpendicular to the near-parallel rows of the BFs and BBs is presented to indicate estimated rotational polarity. BB patches displaying a "scatter" pattern of BFs, however, did not show apparent rotational polarity. The framed regions were magnified to show details. **d** Illustrations for a typical BB patch in wild-type or *Ccdc57*$^{-/-}$ mTECs. **e**–**g** *Ccdc57* deficiency slightly attenuated tracheal multicilia-driven liquid flows. Living tracheal tissue fragments were dissected from littermates and immersed (epithelial face down) in a culture medium containing SiR-tubulin to label cilia, followed by the addition of fluorescent latex beads as tracers of liquid flows (**e**). Motilities of cilia and beads were recorded in the same microscopic field at 10 ms and 100 ms intervals, respectively. Representative results (**f**) are presented by merging image sequences of cilia in the first three frames to show ciliary motilities and of beads in 3 sec to show liquid flows. Colored arrows indicate trajectories of typical rapidly-moving fluorescent puncta during the first 500 ms. Bead velocities (mean ± SD plus sample dots) (**g**) were quantified from 6 microscopic fields of tracheas from two *Ccdc57*$^{-/-}$ P40 mice and 4 microscopic fields of tracheas from two wild-type littermates. 30 traceable rapidly-moving fluorescent puncta were scored in each field. The *P*-value was from an unpaired two-tailed student's *t* test. Source data are provided as a Source Data file.

Ccdc57 appears to function similarly in cells with multicilia that are dispersed throughout the apical surface[18,32,46,50]. Analogous to *Ccdc57*$^{-/-}$ E1 cells, BB patches in *Ccdc57*$^{-/-}$ mTECs tend to be arrested between the scatter and the final alignment stages (Fig. 8a–d). Such defects in full rotational polarity are consistent with a defective BF-AO coupling, though details require future investigations. As BBs in cultured mTECs can achieve full rotational polarity (Fig. 8a)[18], they may possess unique polarization mechanisms. Consistently, studies in bovine trachea reveal that BB polarities and AOs in individual TECs display a gradual shift towards their common directions[8]. Furthermore, while the included angle between the BB polarity and the AO varies between 0° and 30° for most cilia, larger angles (30° to 80°) are present[8], suggesting that even the status of the BF-AO coupling differs among cilia in mature TECs. These special features may explain the relatively mild defects in the rotational polarity of BB patches (Fig. 8c, d) and multicilia-driven liquid flows in *Ccdc57*$^{-/-}$ tracheas (Fig. 8e–g), consistent with the lack of respiratory phenotypes for *Ccdc57*$^{-/-}$ mice.

The disorganized ciliary beats and appearance of hydrocephalus in *ccdc57*-deficient zebrafish[39,43] support our phylogenetic analyses (Fig. 1g, h) that suggest an evolutionarily-conserved role of Ccdc57. The axonemal localization of an exogenous ccdc57, the only localization result presented in zebrafish[43], however, requires validations to exclude the possibility of immunostaining or imaging artifacts. In sharp contrast to our results (Supplementary Fig. 4), both BBs and Dvl1 puncta in *ccdc57*$^{-/-}$ adult zebrafish are dispersed[39]. Whether their dispersions are zebrafish-specific or due to deleterious influences of severe hydrocephalus, as BB patch areas increased in E1 cells of *Ccdc57*$^{-/-}$ mice with severe hydrocephalus (Supplementary Fig. 4e–g), requires future clarifications. In adult zebrafish, *ccdc57* deficiency also results in scoliosis, a phenotype attributed to abnormal cerebrospinal fluid flow-induced Urotensin signaling defects in paraspinal muscles[39,43,51,52]. Interestingly, *Ccdc57*-deficient mice develop kyphosis instead of scoliosis (Fig. 4c, h, i). The positive correlation with the severity of hydrocephalus (Fig. 4) implies that the scoliosis phenotype results from similar pathological mechanisms, and future studies are required to verify this. Mice crawl, zebrafish wiggle, and humans walk. Due to the differences in postures, the irregular mechanical strain on the spine primarily due to defective paraspinal muscle contractions would unlikely bend the mouse spine sideways as in zebrafish and humans[39,51,52].

Future elucidations of machineries ensuring the BF-AO relationship would be crucial for molecular mechanisms underlying the PCP of epithelial motile cilia. As Ccdc57 is likely only a component of a substructure, one focus would be on its additional components and action mechanisms. Interestingly, mammalian Lrrcc1 displays a rotationally-asymmetric localization in centriolar/BB distal lumen[34] that closely resembles that of Ccdc57 (Fig. 3), and *Xenopus* Lrrcc1 is critical for the rotational polarity of BBs[53]. As Lrrcc1 is conserved from *Chlamydomonas* to mammals[34], it might lie upstream of Ccdc57. Another focus would be on cross-talks between axonemal and BB conformations. Possibly, the anisotropic CP apparatus might transduce its geographic information to the peripheral DMTs through radial spokes[1], whereas the CP foot, a Centrin-abundant substructure between the CP bottom region and BB distal lumen[23], might transduce CP's orientation information to the BB. Unique bridges between DMT5 and DMT6 identified in sea urchin flagella[54], should they exist in epithelial motile cilia, would further link the BB polarity to the CP apparatus orientation. While these structural relationships outline possible ways of cross-talks, the detailed interplays will require extensive future investigations.

Methods

All experiments involving mice were performed in compliance with the institutional guidelines of Center for Excellence in Molecular Cell Science (CEMCS), Chinese Academy of Sciences (CAS), and approved by the Institutional Animal Care and Use Committee. The housing, care, and breeding of mice were carried out in the Animal Core Facility of CEMCS.

In the study design and analysis, gender was not considered except in the analysis of fertility as there is no obvious correlation between phenotype and gender.

Plasmids

The cDNA fragments of ciliary proteins were PCR amplified from total cDNAs extracted from cultured mTECs at day 10 post ALI or mEPCs at day 10 post serum starvation. To generate adenoviral constructs expressing GFP-Ccdc57, Dvl2-GFP, or mCherry-Vangl2, the full-length cDNAs of murine Ccdc57 (NM_027745.1), Dvl2 (NM_007888.4), or Vangl2 (NM_033509.4) were PCR-amplified and subcloned into the entry vector pYr-1.1-GFP or pYr-1.1-mCherry (YRBio, China). The positions of the tags for Dvl2 and Vangl2 are referred to previous publications[15,55]. The LR recombination reactions between the entry constructs and the destination vector pAD/BLOCK-It-DEST (YRBio, China) were performed using the LR enzyme mix (Thermo Fisher, 11791020). To generate and purify the antibody for Ccdc57, the cDNA fragments of full-length murine Ccdc57 and Ccdc57 (701-902 aa) were amplified by PCR and subcloned into pET28a or pGEX-4T-1 to express His- or GST-tagged proteins, respectively. All constructs were verified by sequencing. Primers used are listed in Supplementary Table 1.

Mice

Ccdc57$^{Kof/+}$ (C57BL/7 N) mice were purchased from Wellcome Sanger Institute (EM: 05377). *EIIa-Cre* (FVB) mice were obtained from Jackson Laboratory (JAX Strain # 003314). *Ccdc57*$^{-/-}$ mice were generated by crossbreeding *Ccdc57*$^{Kof/+}$ mice with *EIIa-Cre* mice. The mice were housed under specific-pathogen-free (SPF) conditions in cages and a 12/12-hr light/dark photoperiod at 20–26 °C. The humidity of the housing room was maintained at 40–70% humidity. The genotyping was performed through PCR using primers listed in Supplementary Table 1. Genomic DNAs extracted from mouse tails were used as templates.

Phylogenetic analysis and sequence alignments

The phylogenetic tree and taxonomic groups were referred to literatures and Taxonomy Browser of the National Center for Biotechnology Information (NCBI) (https://www.ncbi.nlm.nih.gov/Taxonomy/Browser/wwwtax.cgi). Protein BLAST searches were used to validate the presence or absence of Ccdc57 orthologues in specific species. Non-redundant protein database of a group of organisms at least the size of a genus was searched to confirm the presence or absence of Ccdc57 orthologues, thus the gene. A representative species, usually a model organism or well-studied species, was then chosen for presentation. Publications indicating the presence of epithelial motile cilia in the presented organisms (Fig. 1f) of invertebrates were as follows: lancelets[56], ascidians[57,58], mussels[7,59], sea urchins[60], flat worms[61], sea anemones[60], and trichoplax[25].

A graphical overview of multiple sequence alignments was obtained using COBALT with default settings (https://www.ncbi.nlm.nih.gov/tools/cobalt/). The sequences of Ccdc57 orthologues used were: human (NP_001381599.1), mouse (NP_082021.1), chicken (XP_046785736.1), frog (XP_031750525.1), zebrafish (NP_001188491.2), lamprey (XP_032822803.1), lancelet (XP_035695536.1), ascidian (XP_026694466.1), sea urchin (XP_782064.5), mussel (CAG2255633.1), flatworm (PAA93612.1), sea anemone (XP_020904658.1), and trichoplax (RDD43904.1). This method highlights highly conserved (red) and less conserved (blue) regions or residues based on the relative entropy threshold.

Cell culture and transfection

HEK293T, HEK293A, Hela, and U2OS cells were grown in Dulbecco's modified Eagle's medium (DMEM) (Hyclone) supplemented with 10% fetal bovine serum (FBS) (Ausbian, VS500T). NIH3T3 cells were grown in DMEM medium supplemented with 10% normal goat serum. hTERT-RPE1 and IMCD3 cells were grown in DMEM/F12 medium (GE Healthcare) supplemented with 10% FBS. All media were supplemented with 0.3 mg/ml glutamine (Sigma, G8540), 100 μ/ml penicillin (Solarbio, P8420), and 100 μ/ml streptomycin (Solarbio, S8290). mTECs were isolated from 4-week-old C57BL/6 J mice and cultured as previously described[23].

Multiciliated mEPCs were isolated and cultured as described previously[23,30]. P0 C57BL/6 J mice were anesthetized on ice, and the telencephala were dissected with sharp tweezers (Dumont, 1214Y84) in cold dissection solution (5 mM Hepes, 161 mM NaCl, 5 mM KCl, 1 mM $MgSO_4$, 3.7 mM $CaCl_2$, and 5.5 mM Glucose, pH 7.4) under a stereo microscope. The telencephala were digested in dissection buffer containing 10 U/ml papain (Worthington-Biochem, LS003126), 0.2 mg/ml L-cysteine, 1.5 mM NaOH, 1 mM $CaCl_2$, 0.5 mM EDTA, and 0.15% DNase I (Sigma-Aldrich, D5025) at 37 °C for 30 min. Fresh DMEM medium (GIBCO, 12430-054) supplemented with 10% FBS, 0.3 mg/ml glutamine, 100 μ/ml penicillin, and 100 μ/ml streptomycin was added, and cells were mechanically dissociated by pipetting up and down gently 20 times with a 5 ml pipette. Cells were centrifugated at 400 × *g* at r.t. for 5 min, resuspended in fresh medium, and seeded into the flask (Sigma-Aldrich, L2020) coated with 10 μg/ml Human Plasma Fibronectin (Sigma-Aldrich, FC010). Neurons were shaken off and removed after culturing for 2 days after inoculation. The remaining cells were cultured to 80%–90% confluency and then re-plated into fibronectin-coated 29 mm glass-bottomed dishes (Cellvis, D29-14-1.5-N) for immunofluorescence staining. After cells were cultured to full confluency, FBS was removed from the medium to initiate differentiation. Fresh serum-free media were changed every other day.

Dissection and culture of lateral ventricle walls

Whole mounts (WMs) of lateral ventricle walls were dissected as described[16] with minor modifications. After euthanizing with CO_2, WMs were dissected to a thickness of 500–1000 μm with Vannas Scissors (66VT, 54138B) in pre-warmed (37 °C) dissection solution (25 mM Hepes, 117.2 mM NaCl, 5.3 mM KCl, 0.81 mM $MgSO_4$, 1.8 mM $CaCl_2$, 26.1 mM $NaHCO_3$, 1 mM $NaH_2PO_4{\cdot}2H_2O$, and 5.6 mM Glucose, pH 7.4). The dissected samples were either fixed (refer to the text under the subtitle "Immunofluorescence staining and imaging") or cultured in DMEM medium supplemented with 0.3 mg/ml glutamine, 100 μ/ml penicillin and 100 μ/ml streptomycin. For imaging, the region of interest was the middle region of the anterior-middle area on the WM surface, which was densely populated with multiciliated cells[16].

Adenovirus production and transfection

Adenovirus particles were produced in HEK293A cells as previously described[23]. Adenovirus packaging was carried out according to the Adenovirus Packaging Operation Manual (YRBio, China). Plasmids were linearized by *Pac*I restriction enzyme (NEB) at 37 °C overnight, and the linearized DNAs were transfected into HEK293A cells in 6-well plates to produce the primary adenovirus with lipofectamine 2000 (Thermo Fisher, 11668500). Upon approximately 80% of cells displaying a cytopathic effect (CPE), the culture medium was collected as adenoviral stock. The collected medium was added to a 10 cm dish of HEK293A cells for viral amplification. Once noticeable CPE was observed in the infected HEK293A, both cells and culture medium were harvested. The mixture underwent three freeze-thaw cycles (− 80 °C and 37 °C) and was centrifugated at 400 × *g* for 5 min to remove cell debris. The supernatants were collected and stored at − 80 °C. mEPCs and the WMs were infected using a dilution ratio of 1:1000 or 1:200, respectively.

Immunofluorescence staining and imaging

Immunofluorescent microscopy was carried out as previously described[23]. mEPCs grown on 29 mm glass-bottom dish (Cellvis, D29-14-1.5-N) and WMs (Cellvis, D35-20-1.5-N) were pre-permeabilized with 0.5% Triton X-100 in PBS for 30 sec, followed by fixation with 4% fresh paraformaldehyde (PFA) (Sigma-Aldrich) in PBS for 15 min and permeabilization with 0.5% Triton X-100 in PBS for 15 min. After blocking with blocking solution (4% BSA in TBST) for 1 h, the samples were incubated with primary antibodies in the blocking solution overnight at 4 °C and Alexa Fluor secondary antibodies in the blocking solution at r.t. for 1 h. DAPI (Invitrogen) was used to stain the nucleus. The samples were mounted in ProLong™ (Thermo Fisher, 2273640) to preserve the fluorescence signal. Antibodies used are listed in Supplementary Table 2.

Confocal images were captured with an Olympus Xplore SpinSR10 microscope with UPLAPO OHR 60 × /1.50 Objective and an ORCA-Fusion camera (Hamamatsu). Images were processed with maximum intensity projections. 3D-SIM super-resolution images were acquired using the DeltaVision OMX SR imaging system (GE Healthcare). Before image acquisition, channel alignments were calibrated using anti-Deup1 antibody-decorated deuterosomes simultaneously visualized with secondary antibodies conjugated with Alexa Fluor-488, Cy3, or Alexa Fluor-647 as previously described[32]. The z-axis scanning step was 0.125 μm, and raw images were processed in SoftWoRx 7.0 software by the following procedures: OMX SI Reconstruction, OMX Image Registration, and maximum intensity projection.

High-speed live-cell imaging

Ependymal ciliary motility was recorded as described[16,23], with minor modifications. Thin sections (500–1000 μm) of WMs were dissected and immersed (epithelial face down) into DMEM (GIBCO, 12430-054) supplemented with 0.3 mg/ml glutamine, 100 U/ml penicillin and 100 U/ml streptomycin in glass-bottom dishes. Cilia were labeled with 100 nM SiR-tubulin (Spirochrome, SC002) for 1 h, followed by live imaging. The live-cell imaging was carried out with an Olympus Xplore SpinSR10 microscope equipped with a UPLAPO OHR 60 × /1.50 oil objective, an ORCA-Fusion camera (Hamamatsu), OBIS solid-state Laser, 4000 rpm CSU Disk Speed and an incubation

chamber (37 °C, 5% CO_2, and 80% humidity). The laser power for the SiR-tubulin channel (640 nm) was set to 80% to achieve imaging at 10 ms intervals.

Fluid flow assay was performed as previously described[22] with minor modifications. Briefly, ependyma samples were obtained using a vibratome (Leica, VT1000S) to yield 250 µm thick slices and immersed (epithelial face down) into the culture medium in glass-bottom dishes. The ependymal multicilia were labeled with 100 nM SiR-tubulin for 1 h and fluorescent latex beads (250 nm diameter, Thermo Fisher, F8809) were added to the culture medium at a 1:500 dilution. Time-lapse imaging was recorded with a spinning disk confocal microscope (Nikon, Ti2 Microscope) equipped with S Plan Fluor LWD 20 × C objective optics, Prime 95B (A17G203024) camera. Both the movement of fluorescent latex beads was recorded at 561 nm with 15% power and an exposure time of 50–100 ms), whereas the motility of multicilia was captured at 640 nm with 40% power and an exposure time of 11 ms. The exposure interval was set with "no delay". Images and Supplementary Movies were processed with Fiji.

Tracheal ciliary motility and the flow of fluorescent beads were observed as described[21], with minor modifications. Living tracheal tissue fragments were immersed (epithelial side down) into the solution (25 mM Hepes, 117.2 mM NaCl, 5.3 mM KCl, 0.81 mM $MgSO_4$, 1.8 mM $CaCl_2$, 26.1 mM $NaHCO_3$, 1 mM $NaH_2PO_4{\cdot}2H_2O$, and 5.6 mM Glucose, pH 7.4) containing 100 nM SiR-tubulin in glass-bottom dishes for 1 h, followed by the addition of fluorescent latex beads at a 1:500 dilution. Live imaging was performed using the Olympus Xplore SpinSR10 system described above. Ciliary motilities were captured at 640 nm with 100% laser power at 10 ms intervals, whereas movements of fluorescent beads in the tracheal cavity were recorded at 561 nm with 20% laser power at 100 ms intervals. Images were subsequently processed with Fiji.

Electron microscopy

For scanning electron microscopy (EM), mice were deeply anesthetized with avertin (360 mg/kg body weight, Sigma-Aldrich, T48402) through intraperitoneal injections. Following anesthesia, the WMs from *Ccdc57*$^{+/+}$ or *Ccdc57*$^{-/-}$ mice were dissected after transcardial perfusion with PBS and 4% PFA with an injection pump at a flow rate of 250 ml/h (Smiths Medical, WZS-50F6). The samples were fixed with 4% PFA at 4 °C overnight, post-fixed with 1% OsO_4 in PBS at 4 °C for 1 h, and rinsed three times with PBS at r.t. for 10 min each. Dehydration was carried out using an ethanol series (30, 50, 70, 80, 95, and 100%). Critical point drying (Leica EM CPD300) and metal shadowing (40 mA, 60 s) were performed. Images were captured using a FEI Quanta 250 scanning electron microscope.

For transmission EM, WMs from *Ccdc57*$^{+/+}$ or *Ccdc57*$^{-/-}$ mice were dissected and fixed in 2.5% glutaraldehyde at 4 °C overnight, and post-fixed in 1% OsO_4 at r.t. for 1.5 h. Ethanol dehydration was performed, followed by additional dehydration with 100% ethanol treated with pure acetone. Subsequently, the samples were infiltrated with an acetone-resin mixture at r.t. overnight and embedded in Epon 812 resin at 60 °C for 48 h. Ultrathin sections of 70 nm thickness were obtained using an ultramicrotome (Leica EM PACT2) and stained with 2% uranyl acetate for 15 min, followed by 1% lead citrate staining for 5 min. Serial sections were collected in series on 30 metal mesh grids containing 180–240 ultrathin sections. Images were taken at 80 KV using a Tecnai G2 Spirit Twin transmission electron microscope (FEI), and analyzed with Fiji.

For volume EM, fresh tissues were fixed with 2.5% glutaraldehyde with 0.1 M phosphate buffer (PB, pH 7.4). After rinsing with PB and ddH_2O, the tissues were immersed in 1% OsO_4 and 1.5% potassium ferricyanide solution (Sigma-Aldrich) at r.t. for 1 h. Following a series of washes, the samples were incubated in filtered 1% thiocarbohydrazide solution (Sigma-Aldrich) at r.t. for 20 min, 1% unbuffered OsO_4 solution at 4 °C for 1 h, and 2% uranyl acetate at 4 °C overnight. Dehydration steps were performed through graded ethanol (10 min each at r.t.) followed by pure acetone (2 × 10 min). The samples were infiltrated with the acetone-resin mixture at r.t. and embedded in Epon 812 resin, followed by polymerization at 60 °C for 48 h. Automatic collector of ultrathin sections scanning electron microscopy (AutoCUTS-SEM) was performed as described[45]. 347 serial sections of 70 nm thickness (sections) were collected using an ultramicrotome (Leica, UC7, Germany) with the AutoCUTS device (Zhenjiang Lehua Technology Co.,Ltd, China). The serial sections were automatically acquired by a Helios Nanolab 600i dual-beam SEM (Thermo Fisher) with automated imaging software (AutoSEE) and the iFast software (Thermo Fisher). The image parameters included an accelerating voltage of 2 kV, a beam current of 0.69 nA, a CBS detector, a pixel size of 1.4 nm, and a dwell time of 3 µs. Alignment of serial sections was achieved using the registration function of Fiji.

Preparation of brain tissue section and skeletal staining

Coronal slices of brain tissue were obtained as previously described[35]. After euthanizing with CO_2, mouse brains were sectioned at a thickness of 250 µm using a vibratome. These sections were carefully placed in 35 mm glass-bottom dishes for subsequent imaging. Images were captured with an Olympus SZX16 stereo microscope.

For skeletal staining, skeletons were prepared and stained with Alcian blue and Alizarin Red, as previously described[62] with minor modifications. P0 mice were eviscerated and skin was removed, entire skeletons were fixed in 95% ethanol overnight, followed by dehydration with acetone overnight. Skeletons were stained with 0.3% Alcian blue (Sigma-Aldrich, A5268) in 70% ethanol solution for 24 h, and then stained with 0.1% Alizarin Red ARS (Sigma-Aldrich, A5533) in 95% ethanol solution for 1 h. The specimens were treated with 1% KOH in dH_2O overnight, followed by incubation in the mixed solution (1% KOH: glycerol = 1:1) overnight. Finally, the specimens were stored in 100% glycerol and were ready for imaging.

3D X-ray microscopy and micro-CT imaging

For 3D X-ray microscopy, P48 mice were deeply anesthetized using inhalational isoflurane and scanned using a 3D X-ray microscope (PerkinElmer, IVIS SpectrumCT) with a resolution of 300 µm. P0 mice were eviscerated and fixed with 70% ethanol after removing skin[62]. The skeletons were scanned with a high-resolution 3D X-ray microscope based on micro-computed tomography (micro-CT) technology (Bruker, SkyScan 1272) at a resolution of 9 µm. 3D images were reconstructed using a fixed threshold.

Immunoblotting

To prepare tissue lysates, mouse tissues were lysed in ice-cold RIPA buffer (50 mM Tris-HCl, 150 mM NaCl, 1% NP-40, 0.5% Sodium Deoxycholate, 0.1% SDS, and 1 mM EDTA, pH 7.5) supplemented with a cocktail of protein inhibitors. The samples were homogenized using a glass homogenizer and centrifuged at 12,000 × *g* at 4 °C for 15 min. Supernatants were collected and mixed with an equal volume of 2 × SDS-PAGE loading buffer and boiled at 100 °C for 10 min. Cells were directly lysed in 2 × SDS-PAGE loading buffer and boiled. Proteins separated by SDS-PAGE were transferred onto nitrocellulose membranes (General Electric Company). Protein bands were visualized using Western Lightning Plus ECL (PerkinElmer, NEL104001EA). Antibodies used are listed in Supplementary Table 2.

Measurement of BB polarity, AO, and ciliary beat polarity

BB rotational polarity was analyzed as previously described[15,22]. In cross-sections of transmission EM, BB polarity was depicted by a unit vector extending from the BB center to the vertex of its BF. The mean vector length in a full-sized EM micrograph (2048 pixels × 2048 pixels), containing a minimum of 6 BBs with clearly discernible BFs, was calculated using Microsoft Excel to quantify the rotational polarity. In 3D-

SIM images, the BB polarity was defined by a unit vector extending from the center of the Odf2 or Cep164 rings at the distal end of a BB to the center of Centriolin or γ–tubulin signals at the BF. The mean vector length for BBs within a cell was calculated using Microsoft Excel to determine the rotational polarity.

In transmission EM cross-sections, the AO of a cilium was determined by a vector perpendicular to a line traversing the CP plane and directed from DMT1 towards the middle of DMT 5 and 6[8,63]. The mean angle of these vectors was computed from EM micrographs (2048 pixels × 2048 pixels) that contained at least 6 axonemes with clearly visible ultrastructure and was normalized to 0°. The data are presented as distributions of the mean vector angle[8,63]. The BB polarity was determined as a vector extending from the BB center to the tip of its BF.

The angle of AO relative to BB polarity for a cilium was measured by the angle enclosed by the two vectors described above. We chose a clear axonemal cross-section as close as possible to the BB cross-section with clear BF. 7 cilia from P42 wild-type mice and 6 cilia from *Ccdc57*-deficient littermates were traced in EM cross-sections. In addition, 41 cilia from P4 wild-type mice were traced using AutoCUTS-SEM images.

The direction of the effective stroke was labeled by a unit vector. The mean vector length over the first three video frames (1024 pixels × 882 pixels), containing at least 25 E1 cells, was calculated using Microsoft Excel to quantify the rotational polarity of the ciliary beat.

Radar charts were generated using SigmaPlot 12.5 software.

Quantification and statistical analysis

BB numbers were assessed without knowledge of the genotype and measured from 3D-SIM images using Cep164-positive BBs. The BB center and cell border center were determined using the default setting of the "ROI Manager" function in Fiji.

All experiments, unless otherwise stated, were independently repeated at least twice for both microscopic and biochemical results. Statistical results are presented as mean ± SD. Unpaired two-tailed student's t test was performed by GraphPad Prism 9.0. Differences were considered significant at $P < 0.05$. Data analyses were blinded, with the researchers performing the quantification being unaware of the genotype.

Reporting summary

Further information on research design is available in the Nature Portfolio Reporting Summary linked to this article.

Data availability

All data necessary for evaluating the conclusions of this study are present within the paper and its online supplemental material. Source data are provided in this paper.

References

1. Ishikawa, T. Axoneme structure from motile cilia. *Cold Spring Harb. Perspect. Biol.* **9**, a028076 (2017).
2. Lechtreck, K. F., Sanderson, M. J. & Witman, G. B. High-speed digital imaging of ependymal cilia in the murine brain. *Methods Cell Biol.* **91**, 255–264 (2009).
3. Satir, P. & Christensen, S. T. Overview of structure and function of mammalian cilia. *Annu. Rev. Physiol.* **69**, 377–400 (2007).
4. Samsel, Z., Sekretarska, J., Osinka, A., Wloga, D. & Joachimiak, E. Central apparatus, the molecular kickstarter of ciliary and flagellar nanomachines. *Int. J. Mol. Sci.* **22**, 3013 (2021).
5. Tamm, S. L. & Tamm, S. Ciliary reversal without rotation of axonemal structures in ctenophore comb plates. *J. Cell Biol.* **89**, 495–509 (1981).
6. Lindemann, C. B. & Lesich, K. A. Flagellar and ciliary beating: the proven and the possible. *J. Cell Sci.* **123**, 519–528 (2010).
7. Gibbons, I. R. The relationship between the fine structure and direction of beat in gill cilia of a lamellibranch mollusc. *J. Biophys. Biochem. Cytol.* **11**, 179–205 (1961).
8. Schneiter, M. et al. Multi-scale alignment of respiratory cilia and its relation to mucociliary function. *J. Struct. Biol.* **213**, 107680 (2021).
9. Ohata, S. & Alvarez-Buylla, A. Planar organization of multiciliated ependymal (E1) Cells in the brain ventricular epithelium. *Trends Neurosci.* **39**, 543–551 (2016).
10. Butler, M. T. & Wallingford, J. B. Planar cell polarity in development and disease. *Nat. Rev. Mol. Cell Biol.* **18**, 375–388 (2017).
11. Lyu, Q., Li, Q., Zhou, J. & Zhao, H. Formation and function of multiciliated cells. *J. Cell Biol.* **223**, e202307150 (2024).
12. Nguyen, Q. P. H. et al. Comparative super-resolution mapping of basal feet reveals a modular but distinct architecture in primary and motile cilia. *Dev. Cell* **55**, 209–223 (2020).
13. Clare, D. K. et al. Basal foot MTOC organizes pillar MTs required for coordination of beating cilia. *Nat. Commun.* **5**, 4888 (2014).
14. Wallmeier, J. et al. Motile ciliopathies. *Nat. Rev. Dis. Prim.* **6**, 77 (2020).
15. Guirao, B. et al. Coupling between hydrodynamic forces and planar cell polarity orients mammalian motile cilia. *Nat. Cell Biol.* **12**, 341–350 (2010).
16. Ohata, S. et al. Loss of Dishevelleds disrupts planar polarity in ependymal motile cilia and results in hydrocephalus. *Neuron* **83**, 558–571 (2014).
17. Boutin, C. et al. A dual role for planar cell polarity genes in ciliated cells. *Proc. Natl. Acad. Sci. USA* **111**, E3129–E3138 (2014).
18. Herawati, E. et al. Multiciliated cell basal bodies align in stereotypical patterns coordinated by the apical cytoskeleton. *J. Cell Biol.* **214**, 571–586 (2016).
19. Werner, M. E. et al. Actin and microtubules drive differential aspects of planar cell polarity in multiciliated cells. *J. Cell Biol.* **195**, 19–26 (2011).
20. Takagishi, M. et al. Daple coordinates planar polarized microtubule dynamics in ependymal cells and contributes to hydrocephalus. *Cell Rep.* **20**, 960–972 (2017).
21. Kunimoto, K. et al. Coordinated ciliary beating requires Odf2-mediated polarization of basal bodies via basal feet. *Cell* **148**, 189–200 (2012).
22. Mirzadeh, Z., Han, Y. G., Soriano-Navarro, M., Garcia-Verdugo, J. M. & Alvarez-Buylla, A. Cilia organize ependymal planar polarity. *J. Neurosci.* **30**, 2600–2610 (2010).
23. Zhao, H. et al. Fibrogranular materials function as organizers to ensure the fidelity of multiciliary assembly. *Nat. Commun.* **12**, 1273 (2021).
24. Gurkaslar, H. K., Culfa, E., Arslanhan, M. D., Lince-Faria, M. & Firat-Karalar, E. N. CCDC57 Cooperates with microtubules and microcephaly protein CEP63 and regulates centriole duplication and mitotic progression. *Cell Rep.* **31**, 107630 (2020).
25. Smith, C. L. et al. Novel cell types, neurosecretory cells, and body plan of the early-diverging metazoan Trichoplax adhaerens. *Curr. Biol.* **24**, 1565–1572 (2014).
26. Schierwater, B. & DeSalle, R. Placozoa. *Curr. Biol.* **28**, R97–R98 (2018).
27. Inglis, P. N., Ou, G., Leroux, M. R. & Scholey, J. M. The sensory cilia of Caenorhabditis elegans. *WormBook*, 1–22 https://doi.org/10.1895/wormbook.1.126.2 (2007).
28. Lattao, R., Kovacs, L. & Glover, D. M. The centrioles, centrosomes, basal bodies, and cilia of drosophila melanogaster. *Genetics* **206**, 33–53 (2017).
29. Vincensini, L., Blisnick, T. & Bastin, P. 1001 model organisms to study cilia and flagella. *Biol. Cell* **103**, 109–130 (2011).

30. Delgehyr, N. et al. Ependymal cell differentiation, from monociliated to multiciliated cells. *Methods Cell Biol.* **127**, 19–35 (2015).
31. Zhao, H. et al. Parental centrioles are dispensable for deuterosome formation and function during basal body amplification. *EMBO Rep.* **20**, e46735 (2019).
32. Zhao, H. et al. The Cep63 paralogue Deup1 enables massive de novo centriole biogenesis for vertebrate multiciliogenesis. *Nat. Cell Biol.* **15**, 1434–1444 (2013).
33. Ishikawa, H., Kubo, A., Tsukita, S. & Tsukita, S. Odf2-deficient mother centrioles lack distal/subdistal appendages and the ability to generate primary cilia. *Nat. Cell Biol.* **7**, 517–524 (2005).
34. Gaudin, N. et al. Evolutionary conservation of centriole rotational asymmetry in the human centrosome. *Elife* **11**, e72382 (2022).
35. Chen, Y. et al. Wdr47 Controls neuronal polarization through the camsap family microtubule minus-end-binding proteins. *Cell Rep.* **31**, 107526 (2020).
36. Lakso, M. et al. Efficient in vivo manipulation of mouse genomic sequences at the zygote stage. *Proc. Natl. Acad. Sci. USA* **93**, 5860–5865 (1996).
37. Davy, B. E. & Robinson, M. L. Congenital hydrocephalus in hy3 mice is caused by a frameshift mutation in Hydin, a large novel gene. *Hum. Mol. Genet.* **12**, 1163–1170 (2003).
38. Liu, H. et al. Wdr47, Camsaps, and Katanin cooperate to generate ciliary central microtubules. *Nat. Commun.* **12**, 5796 (2021).
39. Xie, H. et al. Ependymal polarity defects coupled with disorganized ciliary beating drive abnormal cerebrospinal fluid flow and spine curvature in zebrafish. *PLoS Biol.* **21**, e3002008 (2023).
40. Lukinavicius, G. et al. Fluorogenic probes for live-cell imaging of the cytoskeleton. *Nat. Methods* **11**, 731–733 (2014).
41. Liu, T., Jin, X., Prasad, R. M., Sari, Y. & Nauli, S. M. Three types of ependymal cells with intracellular calcium oscillation are characterized by distinct cilia beating properties. *J. Neurosci. Res.* **92**, 1199–1204 (2014).
42. Al Omran, A. J., Saternos, H. C., Liu, T., Nauli, S. M. & AbouAlaiwi, W. A. Live Imaging of the Ependymal Cilia in the Lateral Ventricles of the Mouse Brain. *J. Vis. Exp.* **100**, e52853 (2015).
43. Li, L. et al. Ccdc57 is required for straightening the body axis by regulating ciliary motility in the brain ventricle of zebrafish. *J. Genet. Genom.* **50**, 253–263 (2023).
44. Stevenson, B. R., Siliciano, J. D., Mooseker, M. S. & Goodenough, D. A. Identification of ZO-1: a high molecular weight polypeptide associated with the tight junction (zonula occludens) in a variety of epithelia. *J. Cell Biol.* **103**, 755–766 (1986).
45. Li, X. et al. Large scale three-dimensional reconstruction of an entire Caenorhabditis elegans larva using AutoCUTS-SEM. *J. Struct. Biol.* **200**, 87–96 (2017).
46. Usami, F. M. et al. Intercellular and intracellular cilia orientation is coordinated by CELSR1 and CAMSAP3 in oviduct multi-ciliated cells. *J. Cell Sci.* **134**, jcs257006 (2021).
47. Zheng, J. et al. Microtubule-bundling protein Spef1 enables mammalian ciliary central apparatus formation. *J. Mol. Cell Biol.* **11**, 67–77 (2019).
48. Guirao, B. & Joanny, J. F. Spontaneous creation of macroscopic flow and metachronal waves in an array of cilia. *Biophys. J.* **92**, 1900–1917 (2007).
49. Marshall, W. F. Cilia self-organize in response to planar cell polarity and flow. *Nat. Cell Biol.* **12**, 314–315 (2010).
50. Boutin, C. & Kodjabachian, L. Biology of multiciliated cells. *Curr. Opin. Genet. Dev.* **56**, 1–7 (2019).
51. Zhang, X. L. et al. Cilia-driven cerebrospinal fluid flow directs expression of urotensin neuropeptides to straighten the vertebrate body axis. *Nat. Genet.* **50**, 1666 (2018).
52. Grimes, D. T. et al. Zebrafish models of idiopathic scoliosis link cerebrospinal fluid flow defects to spine curvature. *Science* **352**, 1341–1344 (2016).
53. Nommick, A. et al. Lrrcc1 and Ccdc61 are conserved effectors of multiciliated cell function. *J. Cell Sci.* **135**, jcs258960 (2022).
54. Lin, J., Heuser, T., Song, K., Fu, X. & Nicastro, D. One of the nine doublet microtubules of eukaryotic flagella exhibits unique and partially conserved structures. *PLoS ONE* **7**, e46494 (2012).
55. Park, T. J., Mitchell, B. J., Abitua, P. B., Kintner, C. & Wallingford, J. B. Dishevelled controls apical docking and planar polarization of basal bodies in ciliated epithelial cells. *Nat. Genet.* **40**, 871–879 (2008).
56. Hirakow, R. & Kajita, N. Electron microscopic study of the development of amphioxus, Branchiostoma belcheri tsingtauense: The gastrula. *J. Morphol.* **207**, 37–52 (1991).
57. Konno, A. et al. Distribution and structural diversity of cilia in tadpole larvae of the ascidian Ciona intestinalis. *Dev. Biol.* **337**, 42–62 (2010).
58. Konno, A., Shiba, K., Cai, C. & Inaba, K. Branchial cilia and sperm flagella recruit distinct axonemal components. *PLoS ONE* **10**, e0126005 (2015).
59. Aiello, E. & Sleigh, M. A. The metachronal wave of lateral cilia of Mytilus edulis. *J. Cell Biol.* **54**, 493–506 (1972).
60. Sigg, M. A. et al. Evolutionary proteomics uncovers ancient associations of cilia with signaling pathways. *Dev. Cell* **43**, 744–762 (2017).
61. Rompolas, P., Azimzadeh, J., Marshall, W. F. & King, S. M. Analysis of ciliary assembly and function in planaria. *Methods Enzymol.* **525**, 245–264 (2013).
62. Suo, J. et al. VGLL4 promotes osteoblast differentiation by antagonizing TEADs-inhibited Runx2 transcription. *Sci. Adv.* **6**, eaba4147 (2020).
63. Schatz, G. et al. Ciliary beating plane and wave propagation in the bovine oviduct. *Cells Tissues Organs* **198**, 457–469 (2013).
64. Xu, Y. et al. Characterization of tetratricopeptide repeat-containing proteins critical for cilia formation and function. *PLoS ONE* **10**, e0124378 (2015).
65. Graser, S. et al. Cep164, a novel centriole appendage protein required for primary cilium formation. *J. Cell Biol.* **179**, 321–330 (2007).
66. Ovchinnikov, D. Alcian blue/alizarin red staining of cartilage and bone in mouse. *Cold Spring Harb. Protoc.* **2009**, pdb prot5170 (2009).

Acknowledgements

The authors thank Dr. Fei Sun (Institute of Biophysics, CAS) for advice on AutoCUTS-SEM, Dr. Weiguo Zou, Drs Rui Shao and Jinlong Suo (Institute of Biochemistry and Cell Biology, CAS) for technical assistance on skeletal staining, Kang Kang, Ling Ge, and Jun He (Core Facility for Cell Biology, Institute of Biochemistry and Cell Biology) for technical assistance on 3D X-ray microscopy, micro-CT analysis, and EM studies, Xueke Tan, Zixu Wang, Xiaoyun Zhang and Chunliu Liu (Center for Biological Imaging, Institute of Biophysics) for serial-section collection, imaging, and alignment in AutoCUTS-SEM. This work was supported by the National Natural Science Foundation of China (31991192 for X.Z. and 32230027 for X.Z.).

Author contributions

X.Z. and X.Y. conceived and directed the project. X.P., C.F., and C.S. conducted major experiments. X.L. performed AutoCUTS-SEM. L.X., L.L., and S.H. helped with experiments. X.Z., X.Y., X.P., and C.F. designed experiments, interpreted data, and wrote the manuscript with inputs from all authors.

Competing interests

The authors declare no competing interests.

Additional information

Supplementary information The online version contains supplementary material available at https://doi.org/10.1038/s41467-024-54766-1.

Correspondence and requests for materials should be addressed to Xiumin Yan or Xueliang Zhu.

Peer review information *Nature Communications* thanks the anonymous reviewer(s) for their contribution to the peer review of this work. A peer review file is available.